HHS Public Access

Author manuscript

Nat Cell Biol. Author manuscript; available in PMC 2023 August 01.

Published in final edited form as:

Nat Cell Biol. 2022 August ; 24(8): 1306–1318. doi:10.1038/s41556-022-00961-5.

Single cell analysis of endometriosis reveals a coordinated transcriptional program driving immunotolerance and angiogenesis across eutopic and ectopic tissues

Yuliana Tan[1,2], **William F. Flynn**[1], **Santhosh Sivajothi**[1], **Diane Luo**[1], **Suleyman B. Bozal**[1], **Monica Davé**[1,2], **Anthony A. Luciano**[3], **Paul Robson**[1,2,4,*], **Danielle E. Luciano**[3,*], **Elise T. Courtois**[1,*]

[1]The Jackson Laboratory for Genomic Medicine, Farmington, CT, USA 06032

[2]Department of Genetics and Genome Sciences, University of Connecticut School of Medicine, Farmington, CT, USA 06032

[3]Obstetrics and Gynecology at University of Connecticut, Farmington, CT, USA 06032

[4]Institute for Systems Genomics, University of Connecticut, Farmington, CT, USA 06032

Abstract

Endometriosis is characterized by growth of endometrial-like tissue outside of the uterus affecting many women during their reproductive age, causing years of pelvic pain and potential infertility. Its pathophysiology remains largely unknown, limiting early diagnosis and treatment. We characterized peritoneal and ovarian lesions at single-cell transcriptome resolution and compared to matched eutopic endometrium, control endometrium, and organoids derived from these tissues, generating data on over 122,000 cells across 14 individuals. We spatially localized many of the cell types using imaging mass cytometry. We identify a perivascular mural cell unique to the peritoneal lesions with dual roles in angiogenesis promotion and immune cell trafficking. We define an immunotolerant peritoneal niche, fundamental differences in eutopic endometrium and between lesions microenvironments, and an unreported progenitor-like epithelial cell subpopulation. Altogether, this study provides a holistic view of the endometriosis microenvironment representing a comprehensive cell atlas of the disease in hormonally treated patients, essential information for advancing therapeutics and diagnostics.

[*]Corresponding authors.

Author Contributions

E.T.C., P.R. and D.E.L. conceived and designed the study. Y.T. and E.T.C., performed and supervised the experiments. Y.T. and E.T.C. optimized the tissue dissociation protocol. Y.T., D.L., S.B.B. and E.T.C performed tissue dissociation, FACS sorting and single-cell experiments. D.E.L. and A.A.L. consented patients and collected clinical samples. S.S. performed IMC experiments. M.D performed organoid immunostaining. Y.T., W.F.F., and E.T.C. performed data analysis. Y.T., W.F.F. and E.T.C. wrote the manuscript and generate figures and schematics. Y.T., W.F.F., A.A.L., P.R., D.E.L. and E.T.C., contributed critical data interpretation. All authors have read or provided comments on the manuscript.

Competing Interests

The authors declare no competing interests.

Introduction

Endometriosis is an inflammatory gynecologic condition that affects 10% of women of reproductive age worldwide[1,2], with symptoms including pelvic pain and infertility. It is characterized by the presence of endometrium-like tissue outside of the uterine cavity (termed lesions), commonly found within the peritoneal cavity, as superficial peritoneal or ovarian lesions. Despite the first description of endometriosis occurring almost a century ago, the exact etiology and molecular drivers of the disease remain largely unknown. Limited non-invasive diagnostic tools impede early detection, resulting in up to seven years' delay from onset of symptoms to definitive diagnosis, which currently necessitates invasive surgical biopsies of lesions. Treatment of endometriosis remains similarly challenging, relying on hormonal therapy often in conjunction with surgery. Oral contraceptives aim to reduce symptoms but do not necessarily promote lesion clearance. Even after excision, lesions often recur, and repeated surgery is frequent[3].

Challenges in diagnoses and treatment is, at least in part, due to a poor understanding of the pathophysiology of—and heterogeneity within—endometriosis. The tissue microenvironment, including immune cells, has been highlighted as a critical factor for normal endometrium development and endometriosis progression[4–8]. Advancements in single-cell RNA sequencing (scRNA-seq) and organoid culture systems enable interrogation of the dynamic interactions within the endometrial microenvironment and the cellular complexity and heterogeneity present in endometriosis. Recent studies have demonstrated the power of such cutting-edge technologies to characterize the dynamic changes of human endometrium through the menstrual cycle and pregnancy[5–8].

In this study, we profiled the transcriptomes of endometrium and endometriotic lesions using scRNA-seq and hyperplexed antibody imaging. Our cohorts included patients undergoing oral contraceptive treatment, the most common medical treatment for endometriosis. Consequently, we sought to understand changes within the endometrium and in endometriotic lesions during treatment. Through profiling eutopic endometrium, peritoneal and ovarian lesions, and patient-derived organoids, we uncover distinct cellular changes in endometriosis endometrium as well as specific subsets of immunomodulatory macrophages, immunotolerant dendritic cells (DCs), and vascular changes unique to endometriosis. Our data highlight an unreported endometriosis-specific perivascular population, the presence of tertiary lymphoid structures in some lesions, and a progenitor-like epithelial cell population which may be critical for deeper understanding of this disease.

Results

scRNA-seq and imaging mass cytometry (IMC) tissue analysis.

scRNA-seq was performed on biopsies from 14 individuals. Control eutopic endometrium (Ctrl) represented samples from non-endometriosis patients. Eutopic endometrium (EuE), ectopic peritoneal lesions (EcP) and the adjacent regions to these (EcPA), and ectopic ovarian lesions (EcO) were collected from revised ASRM Stage II-IV patients, the majority under similar hormonal treatment (Fig. 1a, Extended Data Figure 1a, Supplementary Table

1–2). EcPA was included in order to study the environment where lesions establish and evolve.

In total, 108,497 cellular transcriptomes were generated from tissues, with a median 9,186 unique transcripts and 2,823 genes per cell (Fig. 1b). Cells were assigned into five overarching cell types: epithelial, stromal, endothelial, lymphocyte, and myeloid (Fig. 1c,d, Extended Data Figure 1b). Subsequent sub-clustering identified 58 subpopulations (Fig. 1d, Supplementary Table 3), highlighting the cellular complexity of both the endometrium and ectopic lesions. We compared bulk transcriptomes from undissociated tissue to pseudo-bulk single cell transcriptomes to interrogate potential biases (Extended Data Figure 1a). These showed a strong correspondence within each tissue type (Extended Data Figure 1c–d). However, differential expression analysis indicates a few expected cell types are underrepresented in our single-cell dataset (Extended Data Figure 1e, Supplementary Table 4). Nevertheless, similarities between bulk and single-cell transcriptomes indicate that our single-cell dataset reflects much of the original tissue composition and cellular complexity.

The heterogeneity among the profiled tissues is evident in cell type composition changes (Fig 1e, Extended Data Figure 2a). In order to understand spatial organization and potential cell signaling pathways responsible for changes in cell-type proportions, we designed an antibody panel to spatially resolve cell types of interest with IMC (Extended Data Figure 2b).

First, we observed endometrium composition in EuE differs dramatically relative to Ctrl, with much of the epithelial component replaced by stroma and lymphocytes in EuE (Fig. 1e). Consistent with this, we observed a smaller epithelial proportion in EuE compared to Ctrl (Fig. 2a–b, Supplementary Table 2), together with increased expression of cell cycle-related genes and proliferation of endometrial fibroblasts in EuE (Fig. 2c–e). On a per-patient basis, analysis of the scRNA-seq data reveals EuE biopsies stratify into two groups distinguished by immune cell or fibroblast abundance, both distinct from Ctrl samples, and highlights heterogeneity in EuE across patients that exists independent of their hormonal treatment (Fig. 2f, Extended Data Figure 2a). Further, osteoglycin (*OGN*) expression is higher in EuE fibroblasts than Ctrl (Fig. 2g–h, Supplementary Table 5), indicating EuE is transcriptomically and compositionally distinct from Ctrl.

Second, EcP and EcPA are highly similar, particularly among epithelial cells, which suggests that lesions may extend beyond their macroscopic core and into the surrounding peritoneum (Fig 1e,f). Third, the two lesion types display markedly different cellular compositions, confirmed by IMC, where we observed scarce epithelial glands and predominance of stromal cells within EcO when compared to EcP (Fig 1e–g).

Active vascular remodeling and immune cell-trafficking in EcP.

We found endothelial cells (EC) to be markedly increased in EcP, hinting at angiogenesis. We identified cellular components of vasculature: four mural and seven endothelial cell subpopulations, by careful analysis of previously described marker genes[5,6,9–11](Fig. 3a–c). Mural cells, which include vascular smooth muscle (VSMC) and perivascular (Prv) cells, are specialized cells directly interact with ECs providing support and promoting vasculature

stabilization. Mural cells account for roughly 40% of stromal cells in EcPA (Extended Data Figure 3a) and, together with an increased proportion of EC, suggest a highly vascularized microenvironment (Fig.1e). Prv-STEAP4 and Prv-MYH11 were previously identified in the endometrium[6], and we observed an unreported Prv-CCL19 subpopulation expressing both *STEAP4* and *MYH11* (Fig. 3b). This subpopulation accounts for the majority of perivascular cells in EcP and EcPA (Extended Data Figure 3b) and exhibits tissue-specific gene expression (Extended Data Figure 3c,d). Interestingly, *SUSD2*, a marker for endometrial mesenchymal stem cells identified in endometriosis[12], is specifically co-expressed in EcP and EcPA *CCL19*$^{+}$ Prv cells (Extended Data Figure 3d). Prv-CCL19 cells are more abundant in and around peritoneal lesions together with an upregulation of *CCL19* and other known angiogenesis regulators such as Synuclein-γ (*SNCG*)[13] and angiopoietins (*ANGPT1*, *ANGPTL1* and *ANGPT2*)[14]. Similarly, Prv-CCL19 upregulate expression of ligands implicated in T-cell recruitment[15] (*CCL21* and *FGF7*) (Fig. 3d–e, Extended Data Figure 3e). Together, these data show the presence of an endometriosis-specific perivascular subpopulation, likely promoting angiogenesis and immune chemotaxis in peritoneal lesions (Fig. 2f).

To further elucidate the interactions between ECs and Prv-CCL19, we performed ligand-receptor analysis to identify unique interactions involving Prv-CCL19 cells (See Methods and Extended Data Figure 4a); our data indicate EC-tip cells likely respond to *ANGPT1* produced by perivascular cells, an interaction known to induce tube formation and branching[16] (Supplementary Table 6). In endometriosis, *TEK* expression is upregulated while expression of *TIE1*, the anti-angiogenic receptor for angiopoietins[14,17], is downregulated (Fig. 3g). Previous studies have shown that *TEK* pathway activation leads to EC proliferation and activation of a feedback loop through *DLL4-NOTCH* signaling to induce tip EC maturation[18–20]. We found significantly increased expression of cell cycle gene *CCND1* and decreased expression of *DLL4* in EuE, EcP, and EcPA relative to Ctrl (Fig. 3g, Extended Data Figure 4b, Supplementary Table 5), suggesting higher proliferative capacity and sprouting of tip ECs. Contrasting this, the cell cycle arrest gene *BTG2* is upregulated and *DLL4-NOTCH* signaling is maintained in EcO, suggesting inhibition of sprouting tip ECs in ovarian microenvironment.

Immune cell trafficking involves extravasation of immune cells from the blood stream, crossing the ECs barrier into interstitial tissue. Extravasation mainly occurs at the capillary and post-capillary venous (PCV) level[21]. We observed proportions of two PCV subpopulations[10,11], activated PCV (EC-aPCV) and EC-PCV cells proportions, are remarkably increased in EcP and adjacent tissue (Extended Data Figure 4c–d). Genes which regulate immune cell attachment and monocyte trafficking[21]—*PECAM1*, *JAM2*, *VCAM1*, *ICAM1*, *CD99*—and genes associated with EC permeability[22]—*PLVAP, AQP1, CXCL12*—are among significantly upregulated genes in endometriosis EC-aPCV, while *ICAM2* which encodes a tight junction protein responsible for endothelial-to-endothelial cell contact[21] is downregulated (Fig. 3h, Supplementary Table 5). Expression of *AQP1*, which is associated with angiogenesis and migration of endothelial cells[23], is substantially increased in endometriosis EC-PCVs and EC-aPCVs (Extended Data Figure 4e–f). Myeloid and lymphocyte cells are abundant both within and surrounding blood vessels in EcP,

pointing towards immune trafficking activity at this site (Fig. 3i). Together, these data suggest peritoneal lesions possess leaky PCV vasculature.

Thus, our data describe an endometriosis-specific perivascular subtype and emphasize a dynamic orchestration of Prv-CCL19 and PCV endothelial subpopulations, likely promoting angiogenesis and immune cell trafficking in peritoneal endometriosis lesions. This analysis also highlights substantial differences between ovarian and peritoneal lesion microenvironments.

Macrophage contributions to lesion microenvironments.

scRNA-seq uncovered 15 myeloid cell subpopulations (Fig 4a, Extended Data Figure 5a) and 14 lymphocyte subpopulations (Fig. 1d). Myeloid cells, particularly macrophages (Mϕs), have been characterized as central components of the endometriosis ecosystem, playing a key role in the establishment of endometriosis[2]. This, together with our observations indicating an increased abundance of myeloid cells in peritoneal lesions (Fig. 1e), prompted us to investigate macrophage heterogeneity. We identified five Mϕ subpopulations, of which Mϕ1-LYVE1 and Mϕ3-APOE were previously identified by single-cell analysis in other systems[9,24,25]. Tissue-resident macrophage subpopulations (Mϕ1-LYVE1, Mϕ2-peritoneal and Mϕ3-APOE) are distinguished by expression of *FOLR2*—a gene associated with embryonic-derived tissue-resident macrophages[22,26]. Mϕ2-peritoneal cells are exclusive to peritoneal tissue and express *ICAM2*, a known marker for peritoneal macrophages[27]. Mϕ4-infiltrated cells are present in all tissues, express *CLEC5A*, *CCR2*, and *VEGFA*, all markers for blood infiltrated macrophages[28,29], and present similar to monocytes (Fig. 4b,c, Extended Data Figure 5b). RNA velocity trajectory analyses suggest Mϕ3-APOE are more similar to tissue resident Mϕ1-LYVE1 and Mϕ2-peritoneal subpopulations (Fig. 4d, Extended Data Figure 5b). Interestingly, Mϕ5-activated cells appear to arise from both infiltrated and tissue-resident macrophages (Fig. 4b–d). Together, these data illustrate the presence of distinct tissue-resident and blood infiltrated macrophage populations in endometrial and lesion tissues.

The relative abundance of macrophage subpopulations differ dramatically between control and endometriosis; for instance, Mϕ1-LYVE1 and Mϕ5-activated are enriched in endometriosis eutopic endometrium and ectopic tissues, respectively, and most macrophages present in EcO are Mϕ1-LYVE1 (Fig. 4c, Extended Data Figure 5c). Across patients, *LYVE1*$^{+}$ macrophages are enriched in both eutopic and ectopic tissues compared to Ctrl (Fig. 4e). Tissue resident *LYVE1*$^{+}$ macrophages have been previously associated with angiogenesis[22,24], arterial stiffness[30] and anti-inflammatory phenotypes[26]. In agreement, we found that endometriosis Mϕ1-LYVE1 upregulate tolerogenic (*VSIG4*, *RGS1*, *IL10*, *EGFL7, LYVE1*) and angiogenesis-related genes (*THBS1*, *HBEGF*, *PDGFB*, *PDGFC, IGF1*) (Fig. 4f). Furthermore, inflammation and antigen presenting pathways of Mϕ1-LYVE1 are downregulated in endometriosis tissues while angiogenesis pathways are enriched in EcPA (Supplementary Table 7). Mϕ1-LYVE1 localization along the vasculature —but not within—confirms the likely link between angiogenesis and this specific cell population (Fig. 4g). In addition, two genes (*IGF1*, *EMB*) previously shown to promote neurogenesis sprouting in endometriosis[31] and neuromuscular junctions[32] were among the

top upregulated genes in MΦ1-LYVE1 in eutopic and ectopic tissues, suggesting their implication in pain-related mechanisms (Fig. 4f). MΦ4-infiltrated cells, almost completely absent in EcO, presented with pro-tolerogenic features in endometrial tissue, starkly contrasting its pro-inflammatory presentation in control endometrium (Fig. 4h). Altogether, we identified endometriosis-associated changes in multiple macrophage subpopulations, promoting tolerogenic, pro-angiogenic, and pro-neurogenic microenvironments. Moreover, the altered macrophage landscape is shared in endometriosis lesions and eutopic endometrium, affecting both tissue resident and blood infiltrated macrophages.

EcPA DCs adopt an immunomodulatory phenotype.

Among DCs, we classified three *CD1C*$^+$ populations as pre-cDC2, cDC2, and DC3 according to previously reported markers[25,33,34] (Fig 5a). DC proportions varied greatly across patients (Extended Data Figure 6a). However, *CD1C*$^+$ DCs consistently accounted for the majority of the DCs in all tissues (Fig. 5b,c).

Despite studies reporting altered DC proportions in endometriosis[35,36], the field is still lacking a comprehensive characterization of DC heterogeneity. Previous studies suggest DCs maintain themselves within tissue by proliferating under normal conditions but can be bolstered by an influx of blood-derived DCs during periods of heightened immune activity[37]. Our analysis suggests cDC2s derive from pre-DCs, consistent with the substantial number of proliferative pre-cDC2 cells observed (Extended Data Figure 6b–c). The relationship between cDC2s and DC3s appears tissue-specific; both populations seem to derive from an intermediate population in Ctrl (red arrows, Extended Data Figure 6b) co-expressing *FLT3, SIGLEC6,* and *AXL* (DC progenitor- and blood-derived DC-markers[38]). Meanwhile, cDC2 and DC3 subpopulations appear to derive from pre-cDC2s in EcP (Extended Data Figure 6d).

As a possible reservoir for tissue-resident DCs, we further interrogated cDC2 diversity. A cDC2 subset in eutopic endometrium and peritoneal lesions, but not EcO, uniquely expresses *CD207*, a gene expressed by Langerhans cells and immature DCs[39] (Fig. 5d–f). Further analysis revealed two cell states in EcP and EcPA cDC2 populations characterized by mutually exclusive expression of *CD207* and *MSR1* (Fig. 5f,g). Differential gene analysis highlighted *CD207*$^+$ cDC2 cells express genes related to immunogenic DC maturation (*IL18*, *GNLY*, *RUNX3, LTB*)[40–42], whereas *MSR1*$^+$ cDC2s express immunomodulatory genes (*MRC1*, *VSIG4*, *SGK1,* and *PECAM1*)[43–45] (Fig. 5f,h). GSEA analysis of cDC2s across tissues indicated phagocytosis and cytokine-mediated signaling pathways were upregulated in endometriosis tissues (Extended Data Figure 6e). These data suggest disease-specific DC heterogeneity and highlights a potential immunomodulatory role for *MSR1*$^+$ cDC2s in the peritoneum.

Lymphocytes organization and cell-cell communications.

Next, we interrogated lymphocyte diversity and their interactions with other immune subpopulations (Fig. 6a and Extended Data Figure 7a,b). Based on ligand-receptor analysis, we found numerous unique interactions, spatially supported by IMC, between T-cells and various immune subpopulations (Extended Data Figure 7c). Particularly,

interactions between *CD86* (expressed in MΦ1-LYVE1) and *CTLA4* (in T_{Reg}) is upregulated in endometriosis (Fig. 6b, Extended Data Figure 7d, Supplementary Table 6). This interaction is important for T_{Reg} suppression and homeostasis[46], and suggests that macrophages' cooperation with T_{reg}s may be an additional mechanism through which an immunomodulatory microenvironment is promoted in endometriosis. Further, we found that genes associated with T_{Reg} regulatory function are altered between control and endometriosis (Fig. 6c): Ctrl T_{Reg}s express *HAVCR2*, *LAG3, ENTPD1, ICOS, TNFRSF4,* and *CTLA4* while *TIGIT*, *PRDM1* and *CD96* expression is prevalent in endometriosis tissues and EcO specifically. Also noteworthy, ENTPD1—which encodes an important regulator in uterine NK cells promoting immune tolerance and angiogenesis during pregnancy[47]—is upregulated in lesion NK1s (Fig. 6d). Collectively, these changes in gene expression indicate modulation of interactions between the various immune subpopulations in ectopic lesions, though the exact mechanism remains unclear.

We interrogated the immune cell spatial localization among ectopic lesions using IMC. Unexpectedly, we observed a large clusters of immune cells in 2 out of 7 peritoneal lesions that fit the description of tertiary lymphoid structures (TLSs) (Fig. 6e–g). TLSs consist of a germinal center (GC) microarchitecture comprising a central B-cell ($CD20^+$) population surrounded by T-cells ($CD3^+$) and the additional presence of follicular dendritic cells ($PDPN^+$) and antigen-presenting cells (HLA-DRA^+), although TLS maturity can modify its composition and organization. TLSs are present in autoimmune disease, chronic inflammatory disease, and tumors but have never been described in endometriosis[48,49]. We did not observe similar structures in EcO or across all EcP (Fig. 6h,i), suggesting TLS formation may not be a driver of lesions but perhaps a consequence of a sustained inflammatory response. Gene expression analysis of B-cells shows subtle transcriptomic differences among genes related to GC B-cells (*BCL6, SEMA4A* and *CXCR5*[49,50]) (Extended Data Figure 7e), suggesting this phenomenon is variable among peritoneal lesions and between patients. Altogether, these data emphasize the diversity among immune cells co-existing within endometriosis lesions.

Characterization of endometrial MUC5B+ epithelial cells.

We identified ten epithelial populations comprising the endometrial glands and mesothelium (Fig. 7a–c); some have previously been observed in healthy endometrium[5,6] whereas other populations differ substantially or have not been previously observed. Namely, we observed previously unreported mesothelial cells found in ectopic tissue and MUC5B+ epithelial cells (Fig. 7a, Extended Data Figure 8a). Epithelial cell composition in peritoneal lesions reflects that found in the endometrium while EcO epithelial populations are smaller and less diverse (Fig. 7b). This suggests endometrial-like epithelial cells in ovarian and peritoneal lesions may differ in their ability to respond to hormonal or differentiation signals.

The MUC5B+ population is present in both eutopic (4–10% of epithelial cells) and ectopic tissues (< 1%) and uniquely expresses *RUNX3*, *TFF3* and *SAA1* (Fig. 7b and Extended Data Figure 8a). We confirmed their presence in eutopic endometrium through immunohistochemistry and IMC (Fig. 7d and Extended Data Figure 8b). Both trefoil factor 3 (encoded by *TFF3* gene) and serum Amyloid A (encoded by *SAA1* and *SAA2*) have

reported involvement in epithelial restitution, a process initiating mucosal epithelial repair and immune cell recruitment, although details of this mechanism are still unclear[51–53]. SAA is a major modulator of inflammation[54] and known promotor of phagocyte chemotaxis through interaction with its receptor FPR2[55]. *TFF3* upregulation has been linked to endometriosis and inflammation[56]. This prompted us to look for potential interactions involving MUC5B+ cells through ligand-receptor analysis. We found *FPR2* to be uniquely expressed by myeloid cells, particularly monocytes and MΦ4-infiltrated cells (Fig. 7e, Supplementary Table 6) suggesting a potential interaction between MUC5B+ cells and blood-derived myeloid cells. Additionally, we noted the co-expression of *PROM1* and *SIX1* - progenitor cell markers[57,58] - in *in vivo* MUC5B+ cells (Fig. 7b).

To investigate the presence of MUC5B+ cells in *in vitro* cultures, we established endometrial epithelial organoids (EEO) from primary tissue, starting with unselected single-cell suspensions (Fig. 7f). EEOs were maintained in proliferative conditions and subsequently profiled by scRNA-seq, yielding data on 13,326 cells (Extended Data Figure 8d). We combined the EEO dataset with the epithelial single-cell transcriptomes from primary tissue and analyzed them jointly (Fig. 7g). Of the populations identified in the primary tissue, EEO cells distribute along ciliated (14%) and glandular proliferative epithelial cells (11%), with few differences related to their tissue of origin (Extended Data Figure 8e). The largest population of EEO cells (70%) cluster closely between glandular proliferative and *MUC5B*$^{+}$ cells from primary tissue (Fig. 7g, arrow) and expresses markers similar to *MUC5B*$^{+}$ cells *in vivo*, such as *RUNX3, TFF3* and *SAA1* (Extended Data Figure 8f).

The elevated proportion of *MUC5B*$^{+}$ cells in organoid culture led us to further interrogate the role of MUC5B+ cells. Thus, we isolated MUC5B^{+} and MUC5B^{-} epithelial populations from primary tissue and performed live imaging during organoid derivation (Extended Data Figure 9a). Organoids derived from MUC5B^{+} cells grow significantly larger and in higher numbers than those of MUC5B^{-} cells (Extended Data Figure 9b–c). Remarkably, MUC5B expression was confirmed in organoids derived from both populations (Extended Data Figure 9d). Altogether these data suggest that MUC5B+ epithelial cells may potentially represent a progenitor-like population.

Discussion

We report a comprehensive description of peritoneal and ovarian endometriosis lesions at single-cell resolution and compare this data to control endometrium, endometrium from endometriosis patients, and organoids derived from these tissues. Our approach was holistic, capturing all cell types (or at least those that survive dissociation) that comprise lesions and their adjacent surroundings and thus providing a view of cellular composition and communication within the niche where lesions establish and evolve. We utilized histopathological imaging and hyperplex antibody-based imaging, with selection of antibodies guided by scRNA-seq, to provide a spatial context.

Our data is generated from patients undergoing lesion excision for endometriosis symptom relief and under hormonal treatment, thus representative of the vast majority of patients, as hormonal therapy is the most frequent management strategy for the condition. This

continuous low-dose estrogen and/or progestin hormonal treatment comprise the bulk of our control cohort as well. Hormonal treatment induces systemic histological and molecular changes that vary from patient to patient and differ substantially from the cyclic changes observed during the normal menstrual cycle. Our study was specifically designed to interrogate transcriptional and compositional differences between control endometrium and endometriosis, irrespective of hormonal treatment. Indeed, despite the inherent patient-to-patient variability in treatment and clinical history common to human studies, we confirmed robust differences between the two tissues, such as *OGN* upregulation and increased stromal cell presence.

As lesions are described as a piece of endometrial tissue identical to the eutopic endometrium, it was not surprising we identified extensive similarities in cell type composition between the eutopic endometrium and peritoneal lesions. We also detected profound dysregulation of the innate immune and vascular systems in peritoneal lesions. Ovarian lesions, however, display extensive and distinct compositional and gene expression differences relative to peritoneal lesions. Our study provides important clues on the interconnected cellular networks where myeloid, endothelial, epithelial, and perivascular subpopulations influence the formation of the endometriosis-favoring microenvironment (Extended Data Figure 10).

Among myeloid cell subpopulations, macrophages and DCs have been described as key players in endometriosis pathology[1,2,4] with reports showing endometriosis-related alterations of macrophages[29,59] and DCs[35,36]. However, a comprehensive description of myeloid sub-types was previously lacking. Here, we present a precise characterization of immunomodulatory macrophage and DC populations in peritoneal endometriosis that adopt a coordinated immunotolerant phenotype in the endometriosis microenvironment, where DCs expressing *MRC1* and *VSIG4*, potentially promoting immunosurveillance escape, and thus benefiting lesion establishment[60,61]. Such a phenotype was reported in decidual macrophages and associated with fetal tolerance during pregnancy[62,63]. Thus, the present dataset constitutes an ideal starting point to understand how endometriosis may hijack a naturally occurring immunotolerant process to sustain lesion formation and evolution. A deeper understanding of this myeloid compartment in endometriosis is critical, as therapeutics targeting the immune system have been proposed as treatment strategies[2,64,65]. The spatial analysis provided by IMC provides valuable information to understand the full dynamic of cellular interactions. One such example is the intriguing discovery of TLSs in peritoneal lesions. Their role in endometriosis remains to be determined. A functional understanding of each myeloid and lymphoid subpopulation will determine if TLSs constitute key drivers of the disease, and therefore key therapeutic targets, or are simply a byproduct of the continuous inflammation provoked by lesion settlement.

The accumulation of myeloid cells in lesions, together with the presence of *LYVE1*-expressing macrophages near the vasculature, is likely linked with increased vascularization, a distinctive trait of peritoneal lesions, and accentuated in the adjacent tissue surrounding these lesions. *CCL19*$^{+}$ (and *CCL21*$^{+}$) perivascular cells may play a role in this as such cells in primary and secondary lymphoid organs have been shown to play a role in immune cell chemoattraction[66,67]. This population has not been previously described in endometriosis.

Supporting our findings, inhibition of *SNCG,* a marker uniquely expressed by *CCL19*$^{+}$ Prv, prevents endometriosis vascularization and growth[68,69]. The peritoneal angiogenic setting contrasts from the ovarian lesion microenvironment where *CCL19*+ perivascular cells are absent. Thus, while ovarian and peritoneal lesions are currently binned under a common disease name and treatment, we uncover fundamental differences in lesion type that may assist in tailoring lesion-specific therapeutic strategy design such as vascular targeting[70,71] for peritoneal lesions.

Endometrial epithelial glands form integral components for both eutopic endometrium and endometriotic lesions. The characterization of endometrial epithelial stem cells has been challenging due to the dynamic nature of the regenerative endometrium. Recent single-cell driven descriptions of endometrial epithelial cells from healthy endometrium provide important insights into epithelial subpopulations and the associated hormone responses across the menstrual cycle[5,6,72]. The field, however, is still lacking a precise characterization of stem or progenitor epithelial cell populations that could explain epithelial gland establishment and initial lesion formation in ectopic tissues. We describe a previously uncharacterized epithelial cell population expressing *MUC5B* among other specific markers, present in both eutopic and, to a lesser extent, in ectopic tissues. Our success in capturing these cells may be a combination of an optimized tissue dissociation protocol, the use of a hormonally-treated cohort, and/or the speed at which we process these from surgery. However, it remains unclear how this cell subset contributes to endometrial regeneration or the genesis of lesions. Further functional studies will be key to define the precise role of these MUC5B+ cells.

While recent studies have begun to describe endometriosis at single cell resolution[73,74], here we have generated the most comprehensive data set, inclusive of spatial organization, describing the eutopic endometrium and ectopic peritoneal and ovarian endometriosis lesions. This atlas represents a unique tool to understand the key players and the dynamic interplay that constitutes the endometriosis niche in hormonally-treated patients. We believe this dataset will be instrumental for designing effective therapeutic strategies or diagnostic biomarkers to provide some relief to the large group of underserved endometriosis patients.

Online Methods

Human endometrium and endometriosis tissue collection

This study was approved by the Ethics Committee of the Institutional Review Board at University of Connecticut Health Center (UCHC), The Jackson Laboratory, and the Human Research Protection Office of U.S Department of Defense and conducted according to all relevant ethical regulations regarding human participants. Written informed consent was obtained from all participants. All participants consented to share recoded information in public, unrestricted databases. Tissue samples were obtained from UCHC. Pre-menopausal female patients (aged 18 to 49 years old) pre-operatively diagnosed with stage II-IV endometriosis and scheduled for laparoscopic surgery were invited to participate in this study. Endometriosis staging was confirmed at the time of laparoscopy according to the revised American Society for Reproductive Medicine guidelines. The majority of the patients (in both control and endometriosis cohorts) were treated with similar

hormonal treatments at the time of sample collection, and as detailed in Supplementary Table 1. To recruit comparable controls, we chose patients under similar progestin/estrogen therapies and subject to the strict selection criteria we established: no history of inflammatory condition or cancer; presence of hormonal treatment; agematched to endometriosis cohort; visual inspection of absence of endometriosis (via laparoscopy with expert surgical evaluation of endometriosis absence). Matched eutopic endometrium and endometriosis tissues were collected from endometriosis patients (Fig. 1a; Supplementary Fig. 1a, b). Eutopic endometrium was obtained by performing an endometrial biopsy during hysteroscopy. Ectopic peritoneal endometriosis was obtained by resecting the entire endometriosis lesion and adjacent peritoneum ensuring the entire visible lesion was excised. For the control cohort, non-endometriosis eutopic endometrium biopsies were obtained from patients scheduled for surgery who were not suspected to have endometriosis. Complete patient demographic information is provided in Supplementary table 1. Analysis of the endometrium histology was performed on H&E stained tissue sections by UCHC pathologists. Upon resection, fresh tissue was immediately stored in MACS tissue storage solution (Miltenyi, 130–100-008) and kept on ice until processing.

Tissue dissociation for single-cell RNA sequencing

Fresh tissues were immediately processed for scRNA-seq. Ectopic endometriosis lesions from the peritoneum were divided into ectopic lesion (EcP) and ectopic adjacent (EcPA) (Supplementary Fig. 1a). Viable single cells were obtained by mechanical and enzymatic digestion using cold active protease (CAP), following a modified version of the previously described protocol[75]. Briefly, minced tissue was transferred to GentleMACS C tubes (Miltenyi, 130–096-334) containing protease solution (10mg/ml *Bacillus Licheniformis* protease (CAP) (Sigma, P5380) in DPBS supplemented with 5mM CaCl2 and 125U/ml DNaseI (Stemcell, 07900) and incubated in cold water bath (6°C) for 7–10 minutes, performing trituration steps every 2 minutes. After incubation, sample were mechanically dissociated on a Miltenyi GentleMACS Dissociator for 1 minute, twice. Undigested tissue was allowed to settle by gravity for one minute. Single cells within the supernatant were transferred into a collection tube containing wash buffer PBS supplemented with 10% fetal bovine serum (FBS) (Gibco, 10082147), 2mM EDTA, and 2% bovine serum albumin (BSA, Miltenyi 130–091-376). Remaining undissociated tissue was incubated with fresh CAP protease for a total of 20 to 40 minutes, proceeding with a trituration step every 5 minutes and a Miltenyi gentleMACS Dissociator step every 15 minutes. After recovery of single cells, residual undissociated tissue was incubated with PBS supplemented with 1 mg/ml dispase on the Miltenyi gentleMACS Dissociator at 37°C for 15 minutes, and until complete tissue dissociation. Single cells were then pelleted, washed, and filtered through 70μm MACS Smartstrainer (Miltenyi, 130–098-462). Prior to FACS sorting, single cell suspension were stained with propidium iodide (PI) (BD Biosciences, 556364) and calcein violet (Invitrogen, C34858) in FACS buffer (PBS, 2mM EDTA, 2% BSA) and according to manufacturer protocols. Viable cells (propidium iodide negative and calcein violet positive) were sorted using the BD FACS Aria Fusion cell sorter, gated using FACS Diva (9.0.1) and recovered in Advanced DMEM/F12 (Gibco, 12634010) supplemented with 2mM GlutaMAX (Gibco, 35050061), 10mM HEPES (Gibco, 15630080), 20% FBS, 1% BSA. Sorted viable cells were then washed and resuspended with 0.04% BSA in PBS and

assessed for viability using trypan blue staining for subsequent scRNA-seq experiments. The detailed protocol is available at Protocols.io[76].

Endometrial epithelial organoid cultures and cell-hashing for scRNA-seq

Following tissue dissociation and single cell recovery, and after 10x chromium chip loading, remaining single cells were pelleted and resuspended in cold Matrigel (Corning, 356231). Fifty microliter (50 μL) droplet were plated onto 24-well plate wells (Greiner Bio-one, 662102) to generate endometrial epithelial organoids (EEOs). After Matrigel dome solidification, organoid media was added to cover each dome, as previously describe by Boretto et al.[77]. Organoid passaging was performed every 7–10 days and according to the established protocol from Turco et al.[78]. For scRNAseq experiments, organoid cultures between passage 3 and 5 and at day 7–11 after plating were collected, washed twice with wash media (Advanced DMEM/F12, 2mM GlutaMAX, 10mM HEPES, 0.1% BSA), and dissociated into single cells using TrypLE Express (Gibco, 12605010) for 3–5 minutes at 37°C. Cell suspensions were filtered with 40 μm mesh filter to remove debris and cell aggregates. Lastly, cells were washed and resuspended with cell staining buffer (Biolegend, 420201) for hashing with TotalSeq-A anti-human Hashtag reagents (Supplementary Table 8, Biolegend) for 30 min at 4°C and following previously published protocol[79]. After staining, cells were washed to remove excess antibody and resuspended in PBS/0.04% BSA for subsequent counting. Hashed cells were assessed for viability and sorted for viable cells as described below.

Single-cell capture, library preparation, and sequencing

Single cell suspensions were analyzed for viability and counted on a Countess II automated cell counter (Thermo Fisher). A total of 12,000 cells were loaded onto a channel of 10X Chromium microfluidic chips for a targeted cell recovery of 6,000 cells per lane. Single cell capture, barcoding, and library preparation were performed using 10X Chromium v3 chemistry according to manufacturer's protocol (10x Genomics, CG000183). Sample cDNA and library quality controls were performed using the Agilent 4200 TapeStation instrument and quantified by qPCR (Kapa Biosystems/Roche). Libraries were sequenced on a NovaSeq 6000 (Illumina) with the S2 100 cycle kit targeting 100,000 reads per cell for tissues or 50,000 reads per cell for organoids.

Single-cell data preprocessing and clustering

Illumina base call files for all libraries were demultiplexed and converted to FASTQs using bcl2fastq v2.20.0.422 (Illumina). The CellRanger pipeline (10x Genomics, version 3.1.0) was used to align reads to the human reference GRCh38.p13 (GRCh38 10x Genomics reference 3.0.0), deduplicate reads, call cells, and generate cell by gene digital counts matrices for each library. The resultant counts matrices were further processed with Scanpy package (version 1.7.1)[80] to exclude genes that are detected in less than 3 cells and to exclude cells with (1) fewer than 500 genes, (2) fewer than 1,000 UMIs, (3) maximum of 100,000 UMIs, and (4) maximum mitochondrial content of 25%. Doublet identification were performed using Scrublet[81]. Filtered matrices were then combined and normalized such that the number of UMI in each cell is equal to the median UMI across the dataset and log transformed. Scanpy was used to identify the top 2,000 highly variable genes

from log transformed combined matrix. The (1) mitochondrial genes, (2) hemoglobin genes, (3) ribosomal genes, (4) cell cycle genes[82], and (5) stress response genes were excluded from highly variable gene set[83]. Principal component analysis and neighborhood graph generation were performed based on highly variable genes set. Harmony (version 1.0) batch correction was performed to reduce variabilities introduced by inherent patient differences, tissue types, and endometriosis staging to enhance clustering by major cell type[84]. For subsequent clustering of each major cell type, batch correction was performed to account only for inherent patient differences and/or endometriosis staging to preserved tissue types specific expression[85]. Batched-corrected principal components were used for dimensionality reduction using Uniform Manifold Approximation and Projection (UMAP). Clustering was then performed with Leiden community detection algorithm[86,87]. Further doublet identification was calculated based on the median distance of a cell to the center of its respective cluster centroid in UMAP space and the coexpression of marker genes of two or more cell types. All suspected doublets were removed from the analysis.

Cell types and cell state identification

Marker genes of each cluster were identified using Wilcoxon Rank-Sum test in a one-versus-rest fashion, with (1) minimum 0.5 – 2 fold change between group, (2) expressed by at least 0.7 fraction of cells in the group, and (3) expressed by maximum 0.3 fraction of cells outside the group. Cell types were determined by matching the biomarkers with previously described cell types and cell states, and from biomarkers curated from the literature (Supplementary Table 3).

Comparative analysis with Bulk RNA-seq

In order to assess possible biases in cellular diversity or transcript capture in the droplet-based scRNA-seq, we performed bulk RNA-seq on tissue-type-matched aliquots of 6 patients from the scRNA-seq cohort as well as 9 additional patients. In total, we collected 12 eutopic, 6 ovarian lesions, and 6 peritoneal lesions bulk RNA-seq samples (Supplementary Table 2). Total RNA of endometrium and endometriotic lesions was extracted from snap frozen tissue or RNAlater (Invitrogen, #AM7020) stabilized tissue using QIAGEN RNeasy Mini Kit according to the manufacturer's instructions. Library preparation was performed using KAPA mRNA Hyperprep kit (Roche) according to manufacturer's instruction. Bulk RNAseq libraries were sequenced on NovaSeq 6000 (Illumina) with SP 100 cycles single-end reads kit resulting in an average of 38.9 million reads per sample. Reads were aligned to the GRCh38.p13 reference genome (GRCh38 10x Genomics reference 3.0.0), filtered, and quantified with nf-core/rnaseq (version 1.4.2)[88] utilizing the STAR aligner. Read counts were normalized to counts per millions (CPM) reads. scRNA-seq was compared to bulk RNAseq by utilizing pseudo-bulk transform (summing UMI counts for all cells in each sample and CPM normalization. For each tissue type, we compared these bulk transcriptomes with pseudo-bulk scRNA-seq profiles of the same type (Extended data Figure 1). Briefly, we computed the spearman correlation for each pairwise combination (n=144 Eutopic, n=24 Ovarian, n=90 peritoneal) of bulk RNA-seq transcriptome and pseudo-bulk transcriptome, shown in Extended Data Figure 1a; spearman correlation helps minimize unwanted biases derived from differences in total mRNA abundance and differences in normalization strategies between pseudo-bulk and bulk expression profiles. Then we

computed the spearman correlation between the mean bulk and single cell pseudo-bulk expression profiles across samples sharing the same sample type (shown in Extended Data Figure 1b). Differential gene expression between scRNA-seq and bulk RNA-seq data was analyzed with edgeR exactTest[89]. Differentially expressed genes (DEGs) were generated sequentially for eutopic endometrium (Control and EuE), ectopic peritoneal endometriosis (EcP and EcPA), and ectopic ovarian endometriosis (EcO) (Supplementary Table 4).

Identification of DEGs and GSEA analysis between tissue types

DEG analysis between tissue types within a population was performed on clusters with more than 500 cells. We utilized edgeR's glmQLFTest function to compare each tissue types to Control samples. Significant DEGs were considered at FDR < 0.01 (Supplementary Table 5). Gene Set Enrichment Analysis (GSEA) to GO Biological process (2018) was performed on significant DEG (FDR < 0.00001) with gseapy (version) prerank function for each cell subtype[90,91]. Resulting enriched gene ontology list was filtered at FDR < 0.10 (Supplementary Table 7).

Correlation matrix, dendrogram, cell cycle phase and cell density estimation

Analyses were executed with functions implemented in Scanpy (1.7.1) package. Similarities between eutopic endometrium (Control and EuE) tissues were based on hierarchical clustering calculated from Pearson correlation using the Ward linkage algorithm. Cell cycle phase (G1, S or G2M) estimation was calculated following the protocol previously described in Satija et al.[92] and based on markers retrieved from Tirosh et al.[93]. The cell density was estimated with Gaussian kernel density estimation on major cell subtype within each tissue type.

Trajectory Inference

Read counts of spliced and unspliced RNA was computed with velocyto (0.17.17)[94] on all 10x libraries obtained from tissue biopsies. We utilized the *run10x* function which takes output from CellRanger pipeline. Reads were aligned to GRCh38 (10x Genomics reference 3.0.0) and GRCh38 repeat mask downloaded from UCSC Genome Browser as recommended. Projected stream and PAGA trajectory was calculated with scVelo (0.2.3) following recommended workflow previously described[95,96]. First, clusters of interest are isolated based on cell barcodes (e.g., myeloid cells in Control). Second, spliced and unspliced counts were log normalized and used for nearest-neighbors estimation. Then, RNA velocity was computed using scVelo's dynamical model which infers the splicing trajectory for each gene and allows for differential kinetics across distinct lineages and functional states that may be present in the dataset. In order to summarize the mRNA velocity computations, we performed PAGA[96] (specifically regarding DC populations). The number of cells per cell type population vary, especially when subset within a single sample type. With the aim of increasing the robustness of the resulting PAGA graphs, we have utilized the following bootstrapping procedure to generate the edges for all PAGA networks presented in this manuscript: starting with the cells derived from one sample type, we generated 100 randomly subsampled datasets such that each cell type population contained 50 cells; populations with fewer than 13 cells were discarded and those with between 13 and 50 cells were supersampled to include 50 cells. We then recomputed the velocyto neighbor

graph, moments distributions, and kinetics, as well as the resulting velocity and PAGA graphs for each randomized dataset[95]. The PAGA connectivities and transitions graphs were used to construct a distribution of linkages between each pairwise combinations of cells. The mean transition probability across these 100 bootstrap samples for each linkage is what is used to plot the PAGA graph, and this process was repeated independently for all sample types comprised by a given group of cell types.

Ligand-receptor analysis

Ligand-receptor analysis was performed using CellPhoneDB (2.1.4)[97] on all 58 subclusters. We modified the protocol by running CellPhoneDB on each 10x library separately to reflect the interactions only within individual tissue sample. As such, we added additional parameters to obtain list of interactions that are (1) p-value < 0.01, (2) detected in at least 50% fraction of each tissue type, (3) is not self-interaction, and (4) is a unique cell-to-cell interactions (number of cell type pair is less than 150 counts, Supplementary Fig. 5). The database of ligand-receptor unique interactions obtained from this analysis is supplied in Supplementary Table 6. The full list of interactions is available at https://github.com/TheJacksonLaboratory/endometriosis-scrnaseq.

Histology and immunofluorescence

Formalin-fixed paraffin-embedded (FFPE) tissues were cut into 5-μm sections, mounted on slides, and stained for hematoxylin and eosin (H/E). The slides were then scanned with a Hamamatsu Nanozoomer slide scanner at 40x magnification for histopathological examination by a pathologist. Cell counting and cell type classification was performed with QuPath (0.3.0) using random forest classifier (Source Data 1). Welch's T-test was performed to obtain p-value. Immunofluorescence staining was performed on FFPE tissue sections. Slides were incubated for 10 minutes at 55°C in a dry oven, deparaffinized in fresh Histoclear (National Diagnostics, #HS-200), and rehydrated through a series of graded alcohols. Antigen retrieval was performed in a decloaking chamber (BioSB TintoRetriever) for 15 minutes at 95°C in neutral citrate buffer, pH 6.00 (Abcam, #ab93678). Tissue was blocked and permeabilized with 10% donkey serum/0.1% Triton X-100 in PBS for 30 minutes at room temperature, then incubated with primary antibodies MUC5B (1/1000, Novus Biologicals, #NBP1–92151) and E-cadherin (5 μg/ml, R&D Systems, #AF648) overnight. Tissue sections were subsequently incubated with secondary antibody Donkey anti-rabbit Alexa Fluor 647 (Invitrogen, #A-31573) and Donkey anti-Goat Alexa Fluor 488 (Invitrogen, #A-11055) for 1 hour at room temperature. DAPI (1 μg/ml, Sigma, MBD0015) was used to counterstain the nuclei, then mounted with ProLong Diamond (Thermo Fisher, #P36970). Images were taken using a Leica SP8 Confocal microscope at 40x magnification using Leica Application Suite X (LAS X) and processed with FIJI[98].

Image Mass Cytometry (IMC)

FFPE of each tissues were cut into 5-μm sections and mounted on slides. Slides were incubated for 15 minutes at 55°C in a dry oven, deparaffinized in fresh histoclear, and rehydrated through a series of graded alcohols. Antigen retrieval was performed in a decloaking chamber (BioSB TintoRetriever) for 15 minutes at 95°C in citrate buffer, pH 6.0. After blocking in buffer containing 3% BSA, slides were incubated overnight at

4°C with a cocktail of metal-conjugated IMC-validated primary antibodies and described in Supplementary table 9. The following day, slides were washed twice in DPBS and counterstained with iridium intercalator (0.25 μmol/L) for 5 minutes at room temperature to visualize the DNA. After a final wash in ddH_20, the slides were air-dried for 20 minutes. The slides were then loaded on the Fluidigm Hyperion imaging mass cytometer. Regions of interest were selected using Fluidigm CyTOF Software (7.0) and ablated by the Hyperion. The resulting images were exported as 16-bit ".tiff" files using the Fluidigm MCDViewer software and analyzed using napari-imc (0.6.4)[99]or the open source Histocat++ (3.0.0) toolbox/ Histocat web[100].

Isolation and characterization of MUC5B+ epithelial population

Fluorescence Activated Cell Sorting (FACS) was performed to isolate $MUC5B^+$ and $MUC5B^-$ epithelial cells from endometrium dissociated tissue (Extended Data Figure 10). Briefly, control eutopic tissue was dissociated as described above. Cells were then stained with PI and with antibodies marking immune cells ($CD45^+$), endothelial cells ($CD31^+$), epithelial cells ($EpCAM^+$), and MUC5B (Supplementary Table 10). We sorted both $MUC5B^+$ and $MUC5B^-$ epithelial cells (BD Bioscience Symphony S6), gated using FACS Diva (9.0.1), and plated 2000 cells of each population in Matrigel domes (Corning, #356231). Growth of organoid was monitored every 4 hours using an Incuycte S5 (Sartorius) live microscope on brightfield imaging for 10 days. Organoid area and counts were analyzed directly in the onboard Incucyte software (Source Data ED9) and a paired t-test was performed with GraphPad PRISM8 for each timepoint.

Statistics and reproducibility

All hypothesis tests were conducted with the Wilcoxon rank-sum test unless otherwise stated, and the Benjamini-Hochberg correction was used to correct for multiple simultaneous hypotheses tests where applicable.

Data availability

RNA–seq data that support the findings of this study have been deposited in the Gene Expression Omnibus (GEO) under accession codes GSE179640. In order to further safeguard patients' genomic identities, SNVs relative to the reference genome are masked in all bam files (BAMboozle v0.5.0)[101]. Moreover, we have made the final single cell datasets available for download and interactive exploration at https://singlecell.jax.org/datasets/endometriosis-2022. For mapping of scRNA-seq and bulk RNA-seq data, GRCh38.p13 (Ensembl Release 93, https://www.ncbi.nlm.nih.gov/assembly/GCF_000001405.27) was used. All other data supporting the findings of this study are available from the corresponding author on reasonable request. Source data are provided with this paper.

Code availability

All code developed for and utilized in this study are available at https://github.com/TheJacksonLaboratory/endometriosis-scrnaseq (temporary link), including modified CellPhoneDB scripts developed to optimize data interpretation for this study.

Extended Data

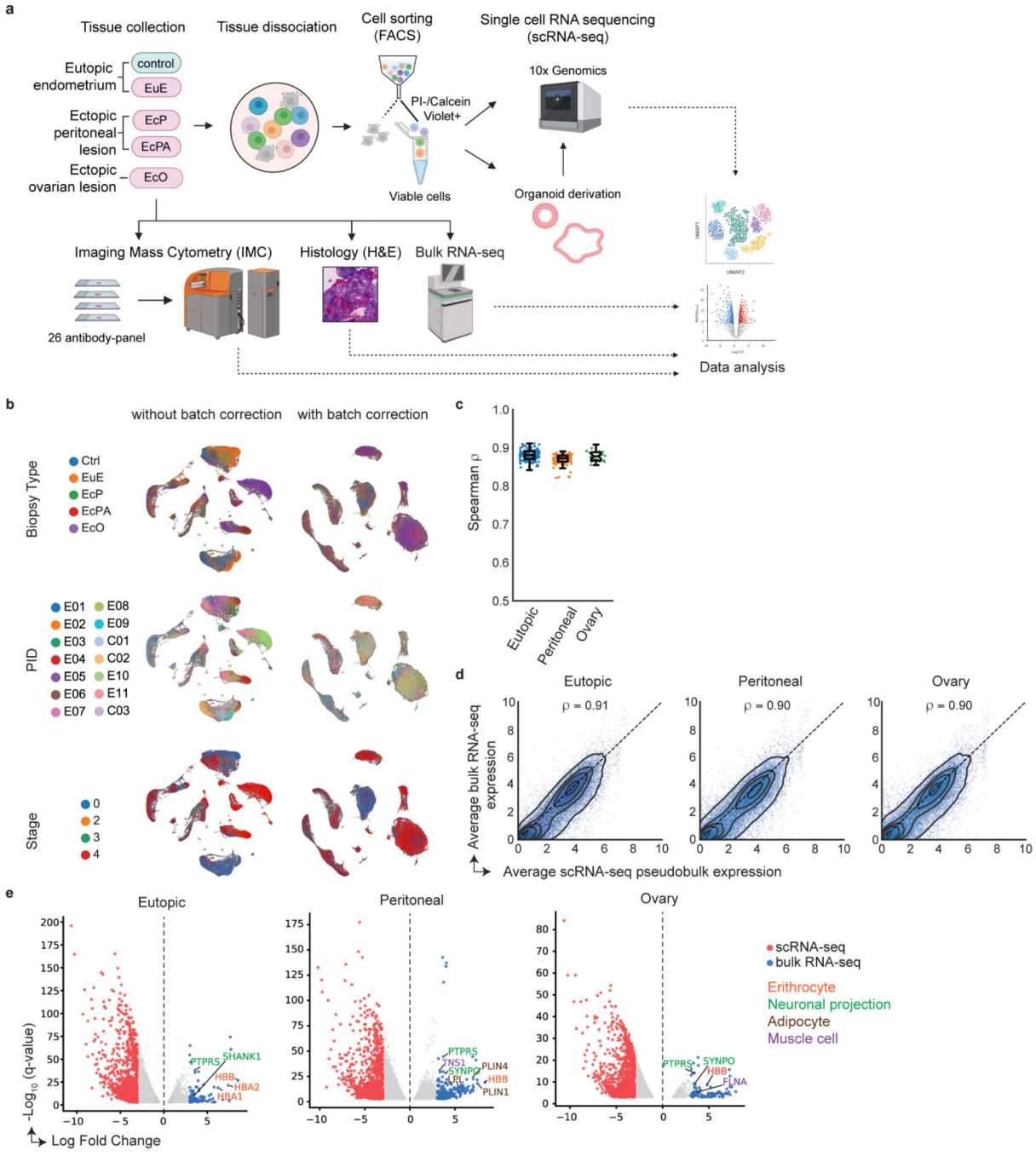

Extended Data Fig. 1. Overview of experiment design and comparison of bulk RNA-seq and scRNA-seq transcriptomic profiles from Ctrl and endometriosis tissues.

a, Experimental workflow. **b**, UMAP showing distribution of cell based on tissue types, PID, and endometriosis stage, before and after batch correction with Harmony. **c**, Box plot showing Spearman's correlation rank (ρ) between bulkRNA-seq and pseudobulk from scRNA-seq in Eutopic (Ctrl & EuE, n = 144), Peritoneal (EcP & EcPA, n =90), or Ovary (EcO, n =24). Each dot represents a sample pair. The box represents the interquartile

range with median and minimum/maximum represented by box centerline and whiskers, respectively. **d**, Scatterplot showing distribution of average gene expression between bulk RNA-seq and scRNA-seq (Spearman ρ). Each dot represents a gene. **e**, Volcano plots representing DEGs between scRNA-seq pseudo bulk (red) and bulk RNA-seq from undissociated tissue (blue) (edgeR, FDR < 0.001, LogFC > 3). The genes highlighted are exclusively expressed in bulk RNA-seq and associated with erythrocytes (orange), neuronal projections (green), adipocytes (brown), and muscle cells (purple). Related to Fig 1.

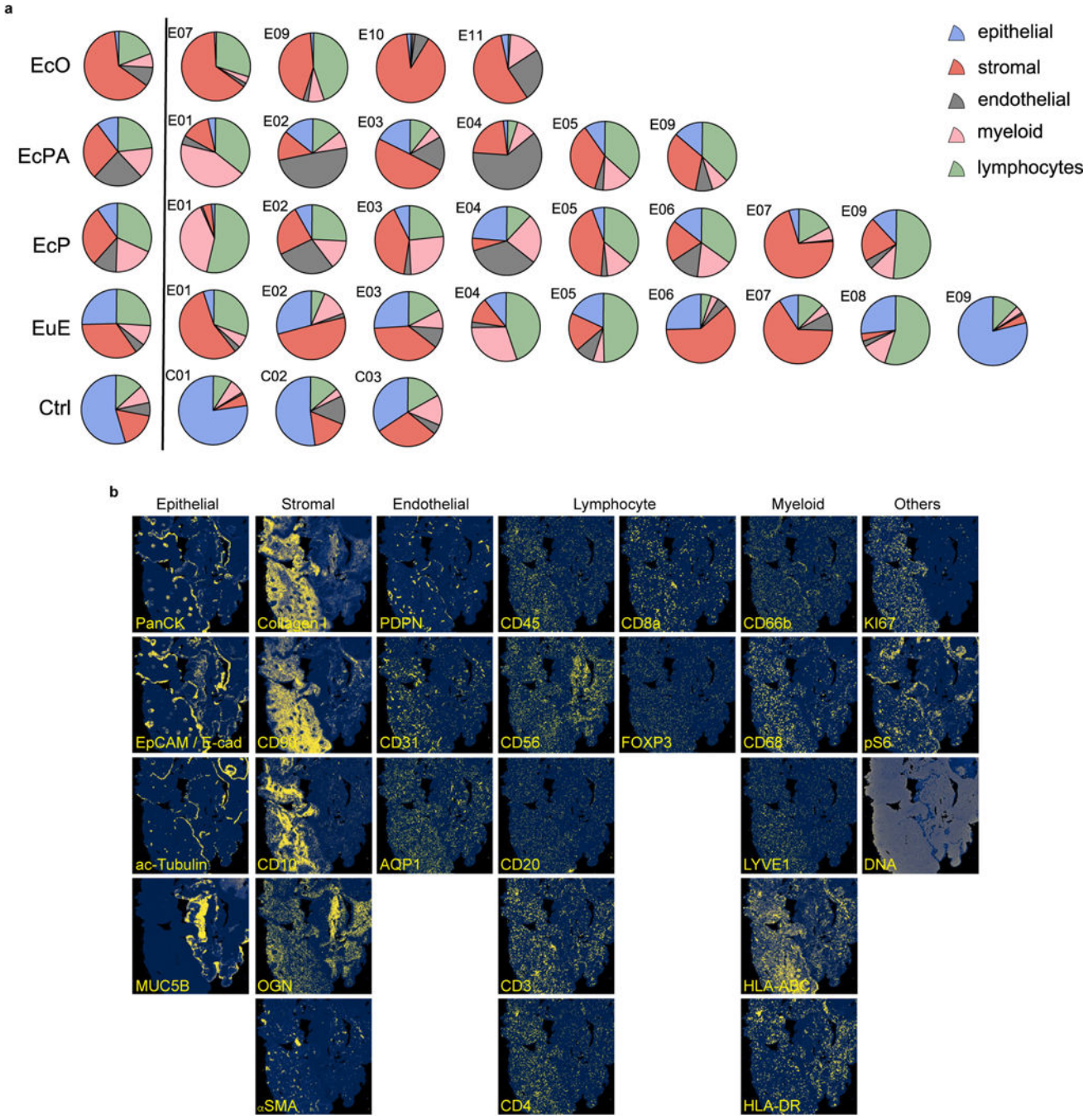

Extended Data Fig. 2. Proportion of major cell types in each replicate and IMC panel for spatial profiling of Ctrl and endometriosis tissues.

a, Major cell types were determined based on UMAP. The mean distribution for all 5 major cell populations is represented for each tissue type Ctrl, EuE, EcP, EcPA, and EcO (left of the line). Each pie chart represents major cell type proportions for each replicate (right of the line). **b**, Each antibody was selected according to the cell types identified by the scRNA-seq data analysis. Representative images show single channels for each metal-conjugated antibody in a EuE biopsy. A total of 26 antibodies was used to identify cellular heterogeneity within stromal, endothelial, epithelial, lymphocyte, and myeloid major cell types. Additional antibodies (in "Others") were used to identify cell proliferation (Ki67), active metabolism (pS6), extracellular matrix (Collagen1), and nuclei (DNA). A complete list of cell subpopulations identified through this panel of markers is listed on Supplementary Table 8b. Related to Fig 1.

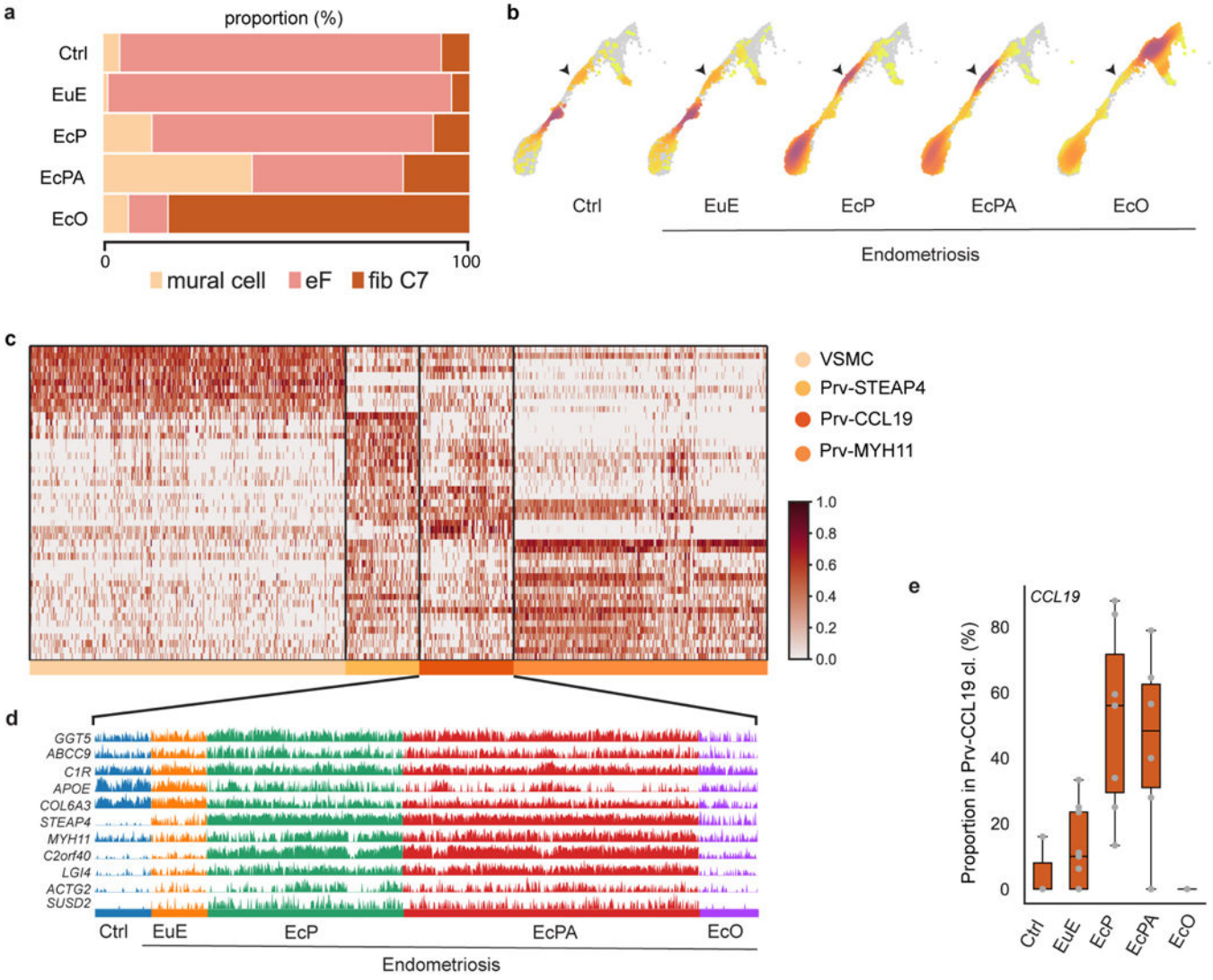

Extended Data Fig. 3. Stromal cell analysis across sample types.

a, Bar plot representing the proportion of stromal cell types in control endometrium and endometriosis lesions. Endometrial fibroblasts were found in all lesions. Fibroblast C7 is the predominant fibroblast type in EcO. **b**, Density plot showing distribution of mural cells for each tissue. Arrows points to Prv-CCL19. **c**, Heatmap of markers genes for mural cell subtypes. **d**, Track plot representing gene expression pattern for selected DEG in Prv-CCL19 subpopulations. *GGT5* and *ABCC9* are pan-markers for this cell subtype. **e**, Box plot showing the proportion of *CCL19*-expressing cells in Prv-CCL19 subpopulation within each tissue type. Each dot represents the percentage of *CCL19*+ cells in a tissue biopsy (Ctrl n = 3, EuE n = 9, EcP n = 8, EcPA n = 6, EcO n = 4). The box represents the interquartile range with median and minimum/maximum represented by box centerline and whiskers, respectively. Related to Fig. 2.

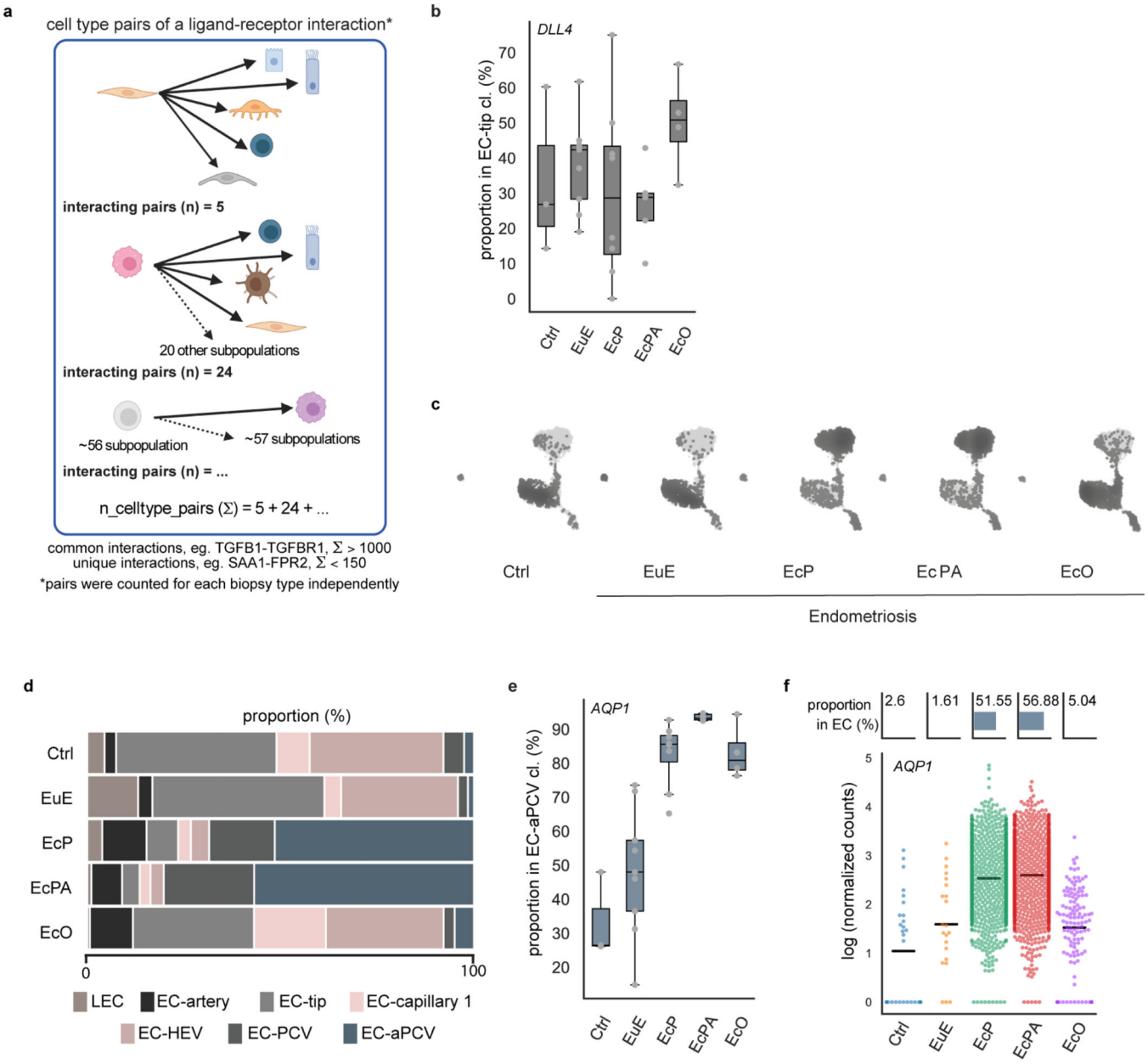

Extended Data Fig. 4. Characterization of endothelial cells (EC) across sample types.

a, Unique cell-to-cell interaction counts obtained from a modified CellPhoneDB procedure. To recover meaningful interactions, we analyzed ligand-receptor interaction in each sample independently. Unique interactions in each tissue type are counted as follows; each ligand-receptor pair observed in a specific cell type pair is counted as one interaction; this is tabulated for all possible pairwise cell type combinations (up to 58 subpopulations in this study) within a sample (n). The total count (Σ, n_celltype_pairs) represents the commonality of the ligand-receptor interaction of interest. The more common interactions (observed in multiple cell type pairs and in all individual samples) will have higher counts while restricted interactions (observed in specific cell type pairs) will have lower counts. We arbitrarily restricted our analysis to interactions observed fewer than 150 times to narrow

the scope of analysis and focus on potentially uncovering unique cell-to-cell interactions. **b**, Box plot showing the proportion of *DLL4*-expressing cells in EC-tip subpopulation within each tissue type. **c**, Density plot showing distribution of endothelial cells for each tissue. **d**, EC proportions by sample type. **e**, *AQP1*+ cell abundance is substantially increased in peritoneal lesions (EcP and EcPA). **f**, (top) Proportion of aPCV among ECs across tissue types. (bottom) Swarm plot showing *AQP1* expression per cell. Horizontal lines represent the median value. For box plots, each dot represents percentage of DLL4+ cells in EC-tip cluster (b) or AQP1+ cells in EC-aPCV cluster (e), in a tissue biopsy (Ctrl n = 3, EuE n = 9, EcP n = 8, EcPA n = 6, EcO n = 4). The box represents the interquartile range with median and minimum/maximum represented by box centerline and whiskers, respectively. Related to Fig. 3.

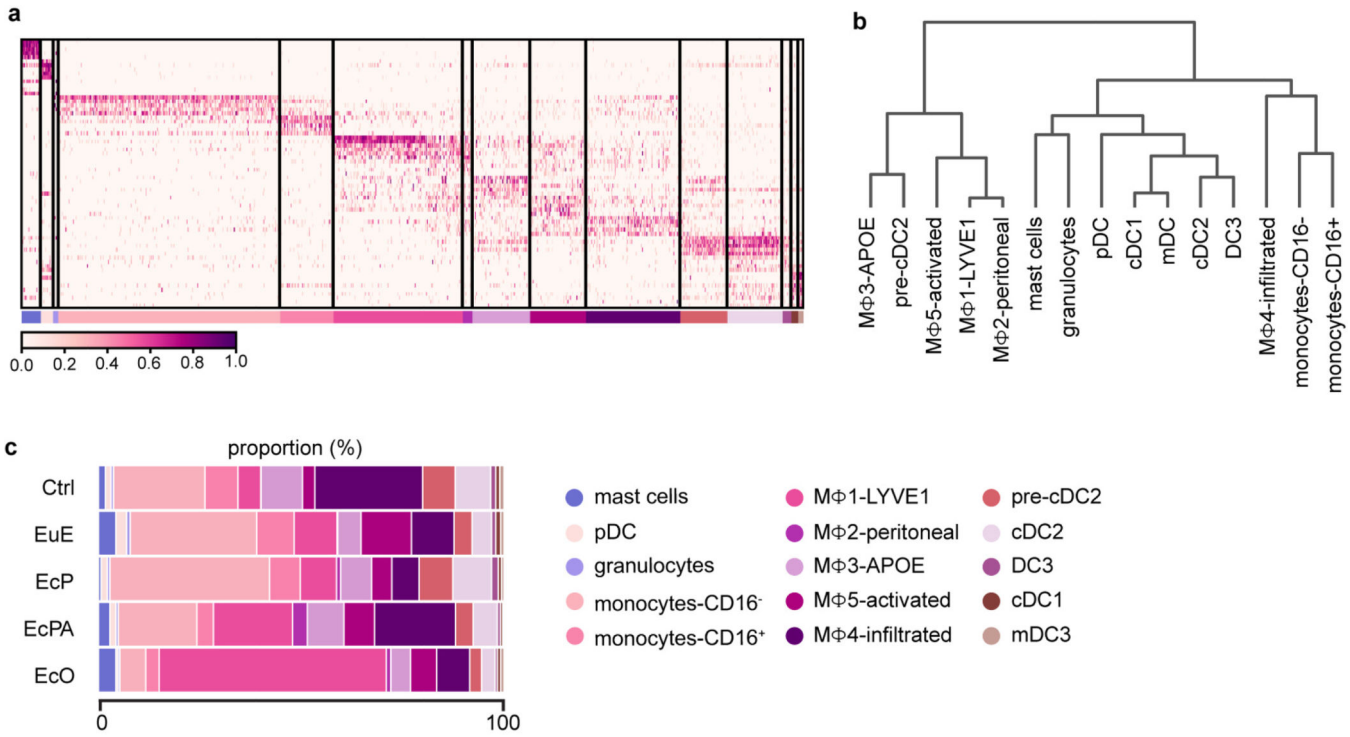

Extended Data Fig. 5. Myeloid cell diversity in control and endometriosis.

a, Heatmap representing marker genes for each myeloid subpopulation. **b,** Dendrogram showing the hierarchical clustering (Pearson correlation) for the myeloid cell clusters. **c,** Bar plot showing the representation of each myeloid subtype across tissue types. Related to Fig. 4.

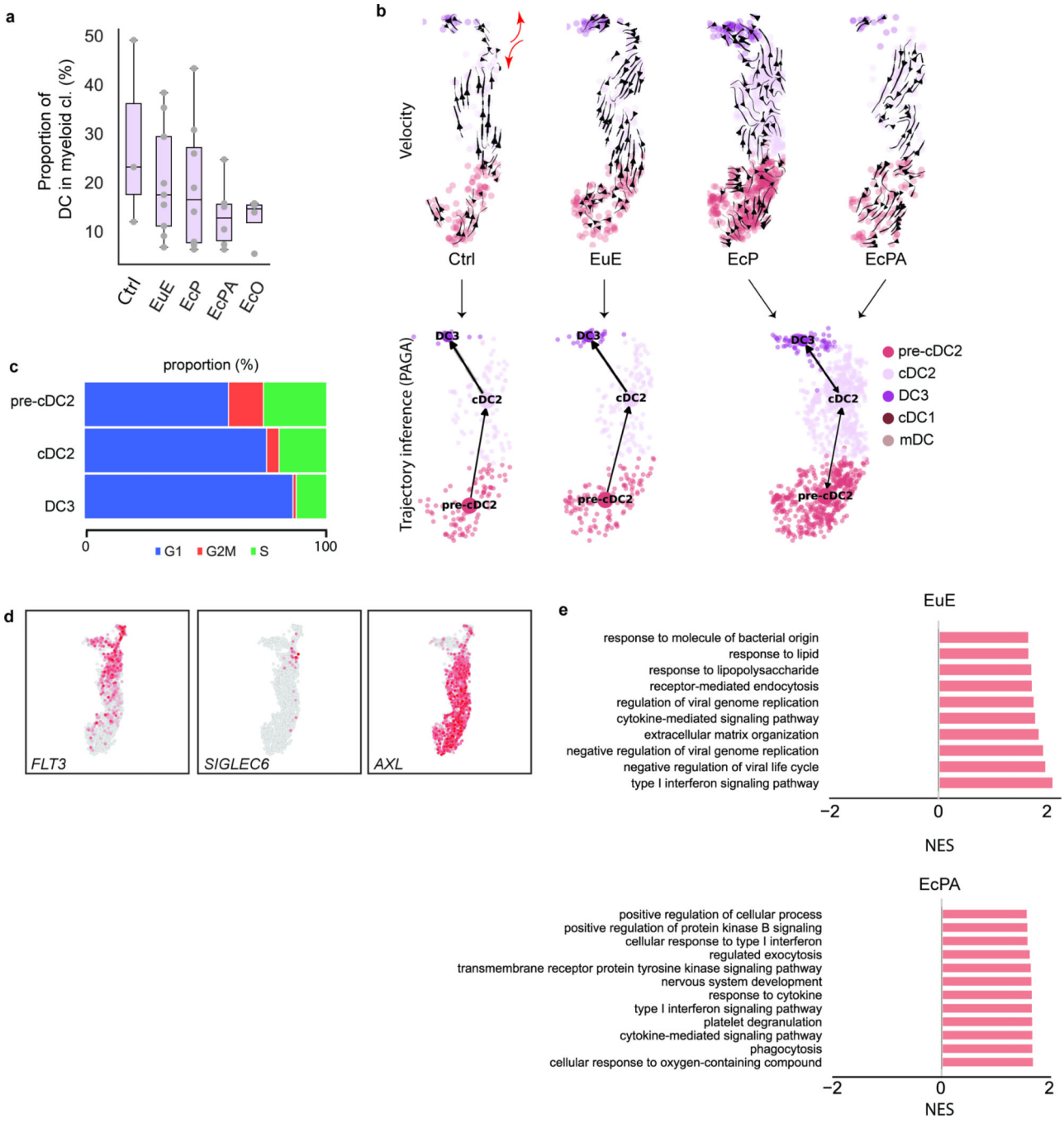

Extended Data Fig. 6. DC subpopulations.

a, Bar plot represents the proportion of DCs among all myeloid cells for each patient (Ctrl n = 3, EuE n = 9, EcP n = 8, EcPA n = 6, EcO n = 4). Patient-to-patient variability was observed in DC proportions within the myeloid population and across different tissue types. The box represents the interquartile range with median and minimum/maximum represented by box centerline and whiskers, respectively. **b**, PAGA and RNA velocity trajectory analyses suggest that pre-cDC2 differentiate towards cDC2 and DC3 in Ctrl and EuE. Red arrows indicate that some cDC2 and DC3 cells derive from a smaller intermediate cell population.

c, Cell cycle analysis for pre-cDC2, cDC2 and DC3 populations. **d**, Expression of DC progenitor markers *FLT3*, *AXL*, and *SIGLEC6*. **e**, Phagocytosis pathway is enriched in cDC2 subpopulations of peritoneal lesions. Bar plot shows the Normalized Enrichment Score (NES) for the top 10- GSEA pathways in cDC2 cells of EuE and EcPA (FDR < 0.1). Related to Fig. 5.

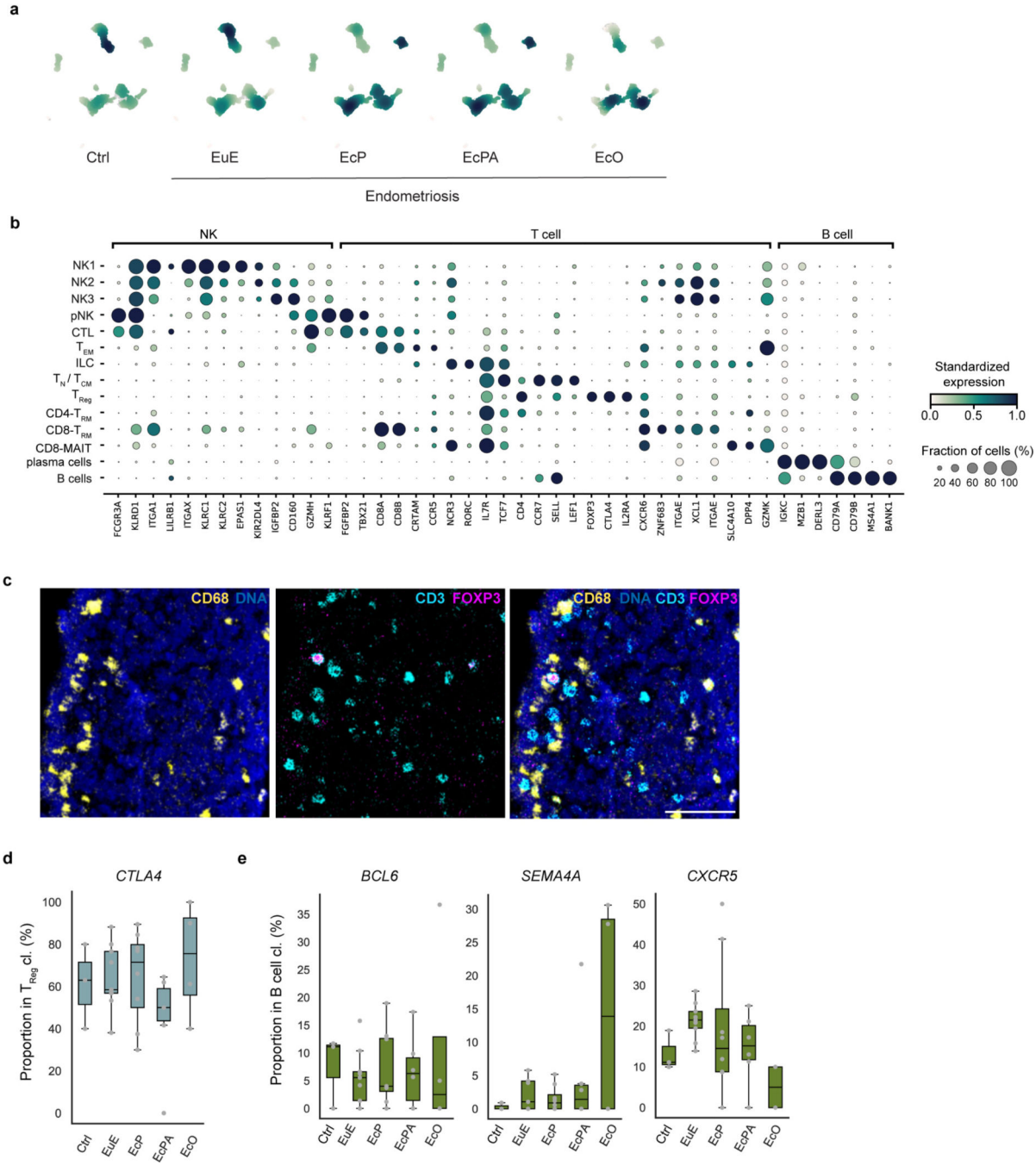

Extended Data Fig. 7. Lymphocyte subpopulations in control and endometriosis tissues.

a, Density plot showing distribution of lymphocyte cells for each tissue. **b,** Dot plot representing marker genes for each lymphocyte subpopulation, including four natural killer cell (NK) clusters, innate lymphoid cells (ILCs), effector memory T-cells (T_{EM}), cytotoxic T-lymphocytes (CTL), naïve/central memory T-cells (T_N/T_{CM}), T regulatory cells (T_{Reg}), CD4- and CD8- tissue resident T cell (CD4-T_{RM} and CD8-T_{RM}, respectively), CD8− mucosal-associated invariant T cells (CD8-MAIT), plasma cells, and B cells. **c,** Representative IMC images showing the presence and proximity of myeloid cells labelled with CD68 (yellow) with T cells labelled with CD3 (cyan), and T_{Reg} labelled with FOXP3 (magenta) in EcO (n = 5); nuclei are marked with DNA intercalation (blue). Scale bar = 100 μm. **d,** Proportion bar plot of *CTLA4* expressing cells from the total T_{Reg} subpopulation. **e,** Proportion box plot of *BCL6*, *SEMA4A*, *CXCR5* expressing cells from the total B cells within each sample type. For box plots, each dot represents a unique patient (Ctrl n = 3, EuE n = 9, EcP n = 8, EcPA n = 6, EcO n = 4). The box represents the interquartile range with median and minimum/maximum represented by box centerline and whiskers, respectively. Related to Fig. 6.

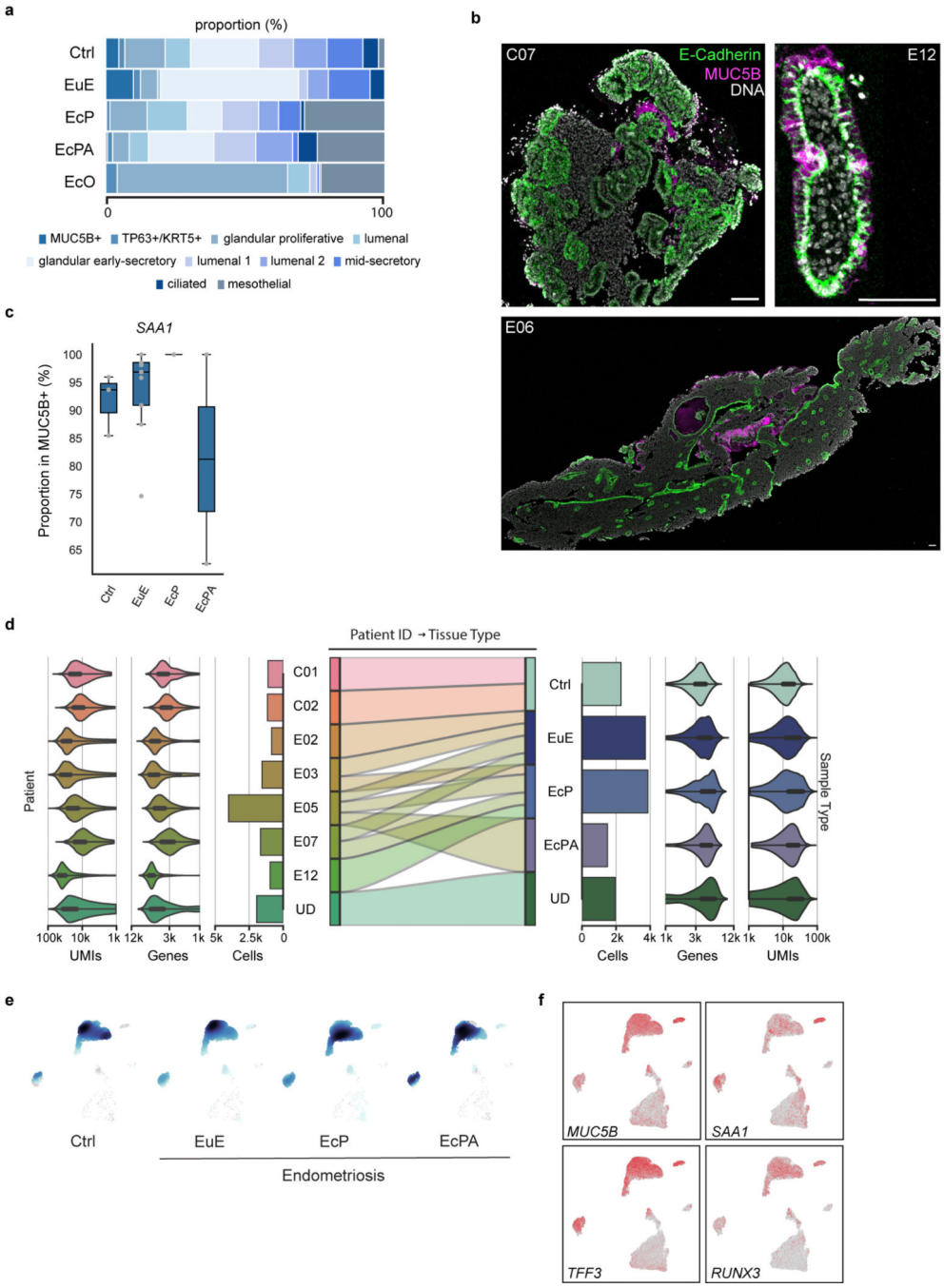

Extended Data Fig. 8. Characterization of *in vivo* epithelial and *in vitro* endometrial epithelial organoid (EEO) cells.

a, Proportions of epithelial subpopulations per sample type. **b,** Representative IMC images of MUC5B+ epithelial cells in eutopic endometrium (Ctrl: C07, EuE: E12, E06) from multiple tissues. Epithelial cells are marked with PanCK, EpCAM, E-cadherin (green); MUC5B (magenta); nuclei (white). Scale bar = 100 μm. **c,** Proportion box plot of *SAA1* expressing cells from the total MUC5B+ cells within each sample type. Each dot represents a unique patient (Ctrl n = 3, EuE n=9, EcP n=8, EcPA n=6, EcO n=4). The box represents

the interquartile range with median and minimum/maximum represented by box centerline and whiskers, respectively. **d**, Sequencing metrics from EEO scRNA-seq; UMIs and unique genes counts are shown for Control (C) and endometriosis (E) patients and across tissue type. Undetermined (UD) group represents single cells which could not be assigned due to the lack of multiplexing hashtag but otherwise passed QC. **e**, Density plot showing distribution of EEO cells derived from Ctrl, EuE, EcP, and EcPA (UD cells were not included). **f**, UMAP showing the co-expression of *MUC5B, SAA1, TFF3,* and *RUNX3* in the MUC5B+ population comprising *in vivo* epithelial cells and EEO. Related to Fig. 7.

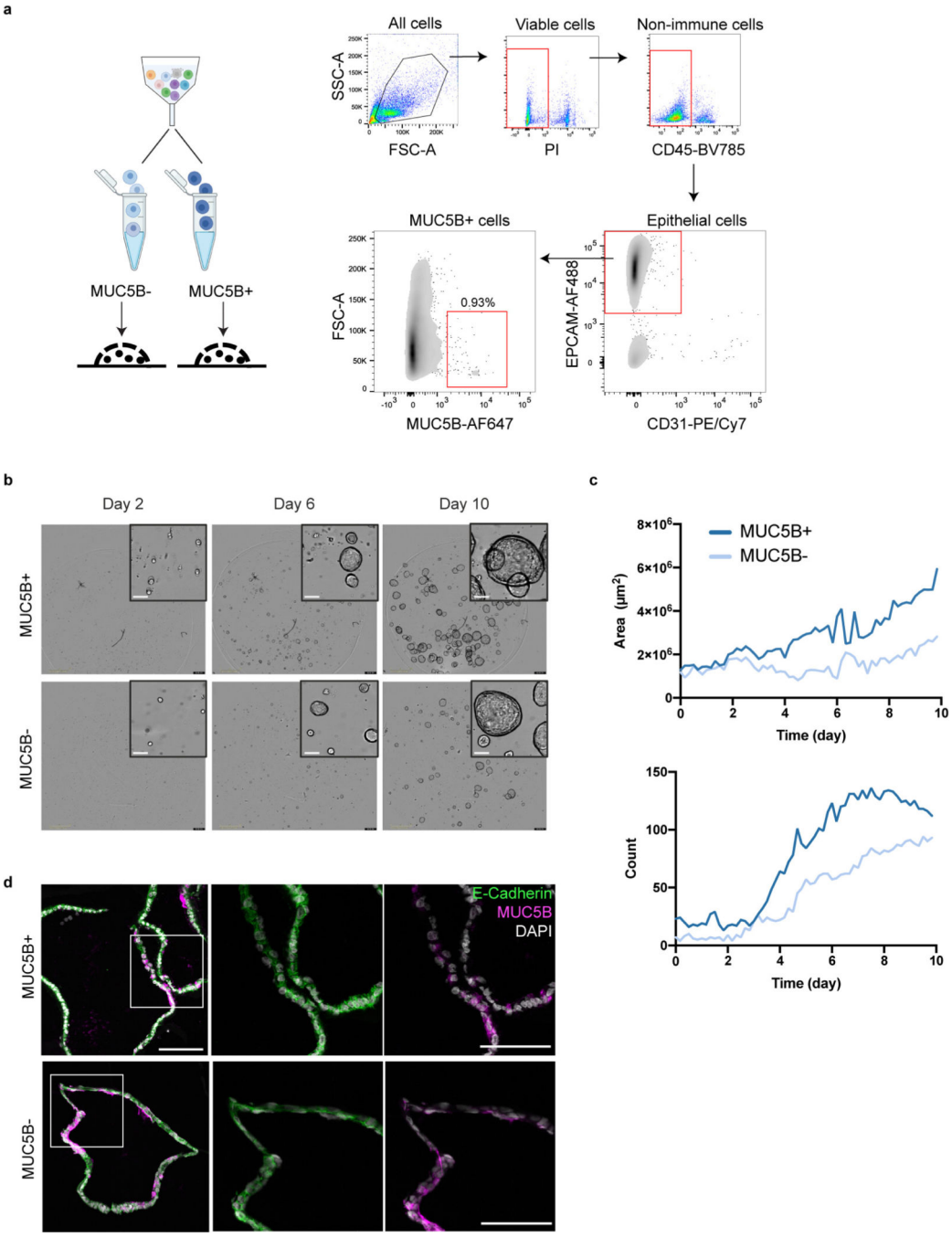

Extended Data Fig. 9. MUC5B+ cells display a progenitor-like capacity in in vitro organoid culture.

A, Schematic and FACS sorting gating strategy to isolate MUC5B+ and MUC5B- epithelial cells from eutopic tissue for organoid generation. B, Representative brightfield images showing the progression of organoid generation from sorted single cells at day 2, 6 and 10. MUC5B+ cells formed EEO faster than MUC5B- cells. Each panel shows a whole Matrigel dome and magnified organoids are shown in the inset. Inset scale bar = 100 μm. c, Line graph showing area (top) and number (bottom) of EEO generated from MUC5B+ (dark blue, n=1) and MUC5B- (sky blue, n=1) cells over time. Area and Count of EEO is significantly

higher in MUC5B+ compared to MUC5B- (paired t-test, two-tailed $p < 0.0001$). d, IF staining of EEO generated from MUC5B+ (n=1) and MUC5B- (n=1) sorted cells showing the co-localization of endometrial epithelial (E-Cadherin, in green) and MUC5B+ (magenta) staining. Nuclei were counterstained with DAPI (gray). Scale bar = 100 μm. Related to Fig. 7.

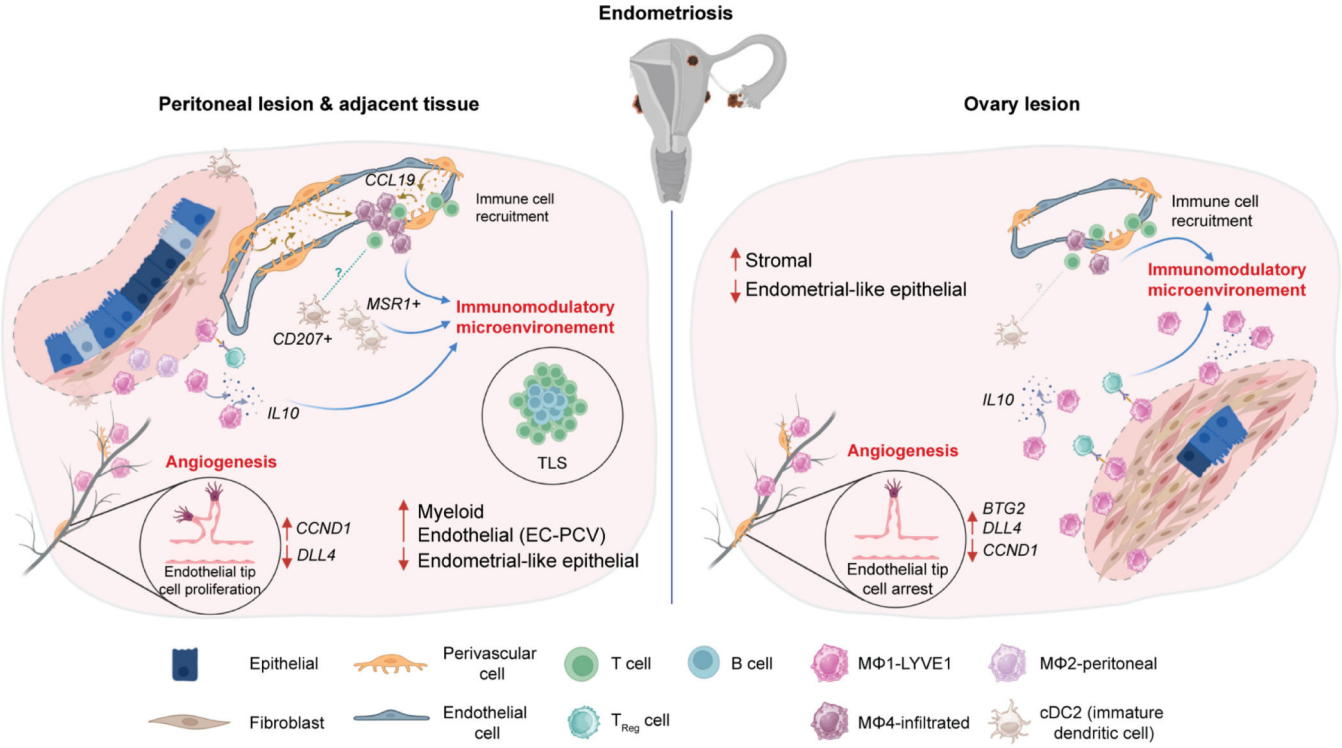

Extended Data Fig. 10. Schematic illustrating the proposed microenvironment alterations for ectopic peritoneal and ovary lesions.

In peritoneal lesion (left), the proportion of myeloid and endothelial is increased, and endometrial-like epithelial population is reduced. CCL19-expressing perivascular cells mediate immune cell recruitment, such as macrophages and T cells, which contributes to the immunomodulatory microenvironment. We observe the presence of MSR1-expressing dendritic cells contributing to immunomodulation. TLS is also observed in some lesions. In addition, Mø1-LYVE1 and perivascular cells contribute to angiogenesis by regulating endothelial tip proliferation. In contrast, ovarian ectopic lesions (right) show a striking increase in the proportion of stromal cell and a reduced endometrial-like-epithelial cell presence. The immunomodulatory microenvironment is mainly driven by Mø1-LYVE1 expressing IL10. In ovary lesions, the regulation of angiogenesis is marked by endothelial cell arrest, resulting in mature vasculature. Created with Biorender.com.

Supplementary Material

Refer to Web version on PubMed Central for supplementary material.

Acknowledgments

The authors would like to thank all participants for their tissue donations and valuable participation in this study. We thank the following Jackson Laboratory (JAX) Scientific Services cores, partially supported through the JAX Cancer Center Support Grant (CCSG) P30CA034196-30, for expert technical assistance: Single Cell Biology, Flow Cytometry and A. Carcio and T. Prosio, Genome Technologies and R. Maurya, Histology, and Microscopy. We also thank the JAX Cyberinfrastructure team for computational resources, L. Perpetua and the UConn Health Research Biorepository, and the UConn Health Surgery Center Personnel for assistance in biopsies collection. We would like to thank the UCHC Pathology and Laboratory Medicine and Mingfu Yu for assistance with histological examination of biopsies. We would like to thank the Clinical and Translational Research Support group, the Sponsored Research Administration service, and the Research Program Development service and Dr. Anna Lisa Lucido for administrative assistance. All schematic panels were created with Biorender.com. This study was supported by the Department of Defense Congressionally Directed Medical Research Programs (CDMRP) Discovery Award Grant W81XWH1910130 (E.T.C.), JAX Institutional startup funds (P.R.) and UCHC/JAX Training Program in Genomic Science T32HG010463 (M.D.). The funders had no role in study design, data collection and analysis, decision to publish or preparation of the manuscript.

References

1. Zondervan KT et al. Endometriosis. Nat. Rev. Dis. Prim 4, 9 (2018). [PubMed: 30026507]
2. Saunders PTK & Horne AW Endometriosis: Etiology, pathobiology, and therapeutic prospects. Cell 184, 2807–2824 (2021). [PubMed: 34048704]
3. Nirgianakis K, Ma L, McKinnon B.& Mueller MD Recurrence Patterns after Surgery in Patients with Different Endometriosis Subtypes: A Long-Term Hospital-Based Cohort Study. J. Clin. Med 9, 496 (2020). [PubMed: 32054117]
4. Symons LK et al. The Immunopathophysiology of Endometriosis. Trends Mol. Med 24, 748–762 (2018). [PubMed: 30054239]
5. Wang W.et al. Single-cell transcriptomic atlas of the human endometrium during the menstrual cycle. Nat. Med 26, 1644–1653 (2020). [PubMed: 32929266]
6. Garcia-Alonso L.et al. Mapping the temporal and spatial dynamics of the human endometrium in vivo and in vitro. Nat. Genet. 2021 5312 53, 1698–1711 (2021). [PubMed: 34857954]
7. Vento-Tormo R.et al. Single-cell reconstruction of the early maternal–fetal interface in humans. Nature 563, 347–353 (2018). [PubMed: 30429548]
8. Lv H.et al. Deciphering the endometrial niche of human thin endometrium at single-cell resolution. Proc. Natl. Acad. Sci 119, e2115912119 (2022).
9. He S.et al. Single-cell transcriptome profiling of an adult human cell atlas of 15 major organs. Genome Biol. 21, 294 (2020). [PubMed: 33287869]
10. Voigt AP et al. Bulk and single-cell gene expression analyses reveal aging human choriocapillaris has pro-inflammatory phenotype. Microvasc. Res 131, 104031 (2020).
11. Goveia J.et al. An Integrated Gene Expression Landscape Profiling Approach to Identify Lung Tumor Endothelial Cell Heterogeneity and Angiogenic Candidates. Cancer Cell 37, 21–36.e13 (2020).
12. Masuda H, Anwar SS, Bühring HJ, Rao JR & Gargett CE A novel marker of human endometrial mesenchymal stem-like cells. Cell Transplant. 21, 2201–2214 (2012). [PubMed: 22469435]
13. Edwards AK, Ramesh S, Singh V.& Tayade C.A peptide inhibitor of synuclein-γ reduces neovascularization of human endometriotic lesions. Mol. Hum. Reprod 20, 1002–1008 (2014). [PubMed: 25024138]
14. Huang H, Bhat A, Woodnutt G.& Lappe R.Targeting the ANGPT-TIE2 pathway in malignancy. Nature Reviews Cancer 10, 575–585 (2010). [PubMed: 20651738]
15. Alpdogan Ö et al. Keratinocyte growth factor (KGF) is required for postnatal thymic regeneration. Blood 107, 2453–2460 (2006). [PubMed: 16304055]
16. Teichert M.et al. Pericyte-expressed Tie2 controls angiogenesis and vessel maturation. Nat. Commun 2017 81 8, 1–12 (2017).
17. Carbone C.et al. Angiopoietin-Like Proteins in Angiogenesis, Inflammation and Cancer. Int. J. Mol. Sci 19, 431 (2018). [PubMed: 29389861]

18. Roca C.& Adams RH Regulation of vascular morphogenesis by Notch signaling. Genes Dev. 21, 2511–2524 (2007). [PubMed: 17938237]
19. Pitulescu ME et al. Dll4 and Notch signalling couples sprouting angiogenesis and artery formation. Nat. Cell Biol 2017 198 19, 915–927 (2017).
20. Mühleder S, Fernández-Chacón M, Garcia-Gonzalez I.& Benedito R.Endothelial sprouting, proliferation, or senescence: tipping the balance from physiology to pathology. Cell. Mol. Life Sci 2020 784 78, 1329–1354 (2020).
21. Wettschureck N, Strilic B.& Offermanns S.Passing the Vascular Barrier: Endothelial Signaling Processes Controlling Extravasation. Physiol. Rev 99, 1467–1525 (2019). [PubMed: 31140373]
22. Sharma A.et al. Onco-fetal Reprogramming of Endothelial Cells Drives Immunosuppressive Macrophages in Hepatocellular Carcinoma. Cell 183, 377–394.e21 (2020).
23. Monzani E, Bazzotti R, Perego C.& La Porta CAM AQP1 Is Not Only a Water Channel: It Contributes to Cell Migration through Lin7/Beta-Catenin. PLoS One 4, e6167 (2009).
24. Chakarov S.et al. Two distinct interstitial macrophage populations coexist across tissues in specific subtissular niches. Science 363, eaau0964 (2019).
25. Cheng S.et al. A pan-cancer single-cell transcriptional atlas of tumor infiltrating myeloid cells. Cell 184, 792–809.e23 (2021).
26. Samaniego R.et al. Folate Receptor β (FRβ) Expression in Tissue-Resident and Tumor-Associated Macrophages Associates with and Depends on the Expression of PU.1. Cells 9, 1445 (2020). [PubMed: 32532019]
27. Kim K-W et al. MHC II+ resident peritoneal and pleural macrophages rely on IRF4 for development from circulating monocytes. J. Exp. Med 213, 1951–1959 (2016). [PubMed: 27551152]
28. Gonzalez-Dominguez E.et al. CD163L1 and CLEC5A discriminate subsets of human resident and inflammatory macrophages in vivo. J. Leukoc. Biol 98, 453–466 (2015). [PubMed: 25877931]
29. Hogg C.et al. Macrophages inhibit and enhance endometriosis depending on their origin. Proc. Natl. Acad. Sci. U. S. A 118, e2013776118 (2021).
30. Lim HY et al. Hyaluronan Receptor LYVE-1-Expressing Macrophages Maintain Arterial Tone through Hyaluronan-Mediated Regulation of Smooth Muscle Cell Collagen. Immunity 49, 326–341.e7 (2018).
31. Forster R.et al. Macrophage-derived insulin-like growth factor-1 is a key neurotrophic and nerve-sensitizing factor in pain associated with endometriosis. FASEB J. 33, 11210–11222 (2019).
32. Lain E.et al. A Novel Role for Embigin to Promote Sprouting of Motor Nerve Terminals at the Neuromuscular Junction. J. Biol. Chem 284, 8930–8939 (2009). [PubMed: 19164284]
33. Villar J.& Segura E.Decoding the Heterogeneity of Human Dendritic Cell Subsets. Trends in Immunology 41, 1062–1071 (2020). [PubMed: 33250080]
34. Maier B.et al. A conserved dendritic-cell regulatory program limits antitumour immunity. Nature 580, 257–262 (2020). [PubMed: 32269339]
35. Schulke L.et al. Dendritic cell populations in the eutopic and ectopic endometrium of women with endometriosis. Hum. Reprod 24, 1695–1703 (2009). [PubMed: 19321495]
36. Hey-Cunningham AJ et al. Comprehensive analysis utilizing flow cytometry and immunohistochemistry reveals inflammatory changes in local endometrial and systemic dendritic cell populations in endometriosis. Hum. Reprod 36, 415–428 (2021). [PubMed: 33313846]
37. Cabeza-Cabrerizo M.et al. Tissue clonality of dendritic cell subsets and emergency DCpoiesis revealed by multicolor fate mapping of DC progenitors. Sci. Immunol 4, eaaw1941 (2019).
38. Karsunky H, Merad M, Cozzio A, Weissman IL & Manz MG Flt3 Ligand Regulates Dendritic Cell Development from Flt3+ Lymphoid and Myeloid-committed Progenitors to Flt3+ Dendritic Cells In Vivo. J. Exp. Med 198, 305–313 (2003). [PubMed: 12874263]
39. Merad M, Ginhoux F.& Collin M.Origin, homeostasis and function of Langerhans cells and other langerin-expressing dendritic cells. Nature Reviews Immunology 8, 935–947 (2008).
40. Tewary P.et al. Granulysin activates antigen-presenting cells through TLR4 and acts as an immune alarmin. Blood 116, 3465–3474 (2010). [PubMed: 20660289]

41. Brown CC et al. Transcriptional Basis of Mouse and Human Dendritic Cell Heterogeneity. Cell 179, 846–863.e24 (2019).
42. Durand M.et al. Human lymphoid organ cDC2 and macrophages play complementary roles in T follicular helper responses. J. Exp. Med 216, 1561–1581 (2019). [PubMed: 31072818]
43. Yi H.et al. Targeting the immunoregulator SRA/CD204 potentiates specific dendritic cell vaccine-induced T-cell response and antitumor immunity. Cancer Res. 71, 6611–6620 (2011). [PubMed: 21914786]
44. Munawara U.et al. Human Dendritic Cells Express the Complement Receptor Immunoglobulin Which Regulates T Cell Responses. Front. Immunol 10, 2892 (2019). [PubMed: 31921153]
45. Schmid E.et al. Serum- and glucocorticoid-inducible kinase 1 sensitive NF-κB signaling in dendritic cells. Cell. Physiol. Biochem 34, 943–954 (2014). [PubMed: 25200670]
46. Halliday N.et al. CD86 Is a Selective CD28 Ligand Supporting FoxP3+ Regulatory T Cell Homeostasis in the Presence of High Levels of CTLA-4. Front. Immunol 11, 3155 (2020).
47. Strunz B.et al. Continuous human uterine NK cell differentiation in response to endometrial regeneration and pregnancy. Sci. Immunol 6, (2021).
48. Aloisi F.& Pujol-Borrell R.Lymphoid neogenesis in chronic inflammatory diseases. Nature Reviews Immunology 6, 205–217 (2006).
49. Cabrita R.et al. Tertiary lymphoid structures improve immunotherapy and survival in melanoma. Nature 577, 561–565 (2020). [PubMed: 31942071]
50. Ruffin A.et al. Divergent cancer etiologies drive distinct B cell signatures and tertiary lymphoid structures. bioRxiv (2020). doi:10.1101/2020.05.29.123265
51. Hinrichs BH et al. Serum Amyloid A1 Is an Epithelial Prorestitutive Factor. Am. J. Pathol 188, 937–949 (2018). [PubMed: 29366677]
52. Taupin D.& Podolsky DK Trefoil factors: initiators of mucosal healing. Nat. Rev. Mol. Cell Biol 2003 49 4, 721–732 (2003).
53. Paulsen FP et al. Intestinal Trefoil Factor/TFF3 Promotes Re-epithelialization of Corneal Wounds. J. Biol. Chem 283, 13418–13427 (2008). [PubMed: 18326859]
54. Cocco E.et al. Serum amyloid A (SAA): A novel biomarker for uterine serous papillary cancer. Br. J. Cancer 101, 335–341 (2009). [PubMed: 19536090]
55. Badolato R.et al. Serum amyloid a is a chemoattractant: Induction migration, adhesion, and tissue infiltration of monocytes and polymorphonuclear leukocytes. J. Exp. Med 180, 203–209 (1994). [PubMed: 7516407]
56. Henze D.et al. Endometriosis Leads to an Increased Trefoil Factor 3 Concentration in the Peritoneal Cavity but Does Not Alter Systemic Levels. Reprod. Sci 24, 258–267 (2017). [PubMed: 27330011]
57. Cindrova-Davies T.et al. Menstrual flow as a non-invasive source of endometrial organoids. Commun. Biol 2021 41 4, 1–8 (2021).
58. Terakawa J.et al. SIX1 cooperates with RUNX1 and SMAD4 in cell fate commitment of Müllerian duct epithelium. Cell Death Differ. 2020 2712 27, 3307–3320 (2020).
59. Maddern J, Grundy L, Castro J.& Brierley SM Pain in Endometriosis. Frontiers in Cellular Neuroscience 14, (2020).
60. Izumi G.et al. Mannose receptor is highly expressed by peritoneal dendritic cells in endometriosis. Fertil. Steril 107, 167–173.e2 (2017).
61. Brech D.et al. A mosaic renal myeloid subtype with T-cell inhibitory and protumoral features is linked to immune escape and survival in clear cell renal cell cancer. bioRxiv (2020). doi:10.1101/2020.01.20.912865
62. Gustafsson C.et al. Gene expression profiling of human decidual macrophages: Evidence for immunosuppressive phenotype. PLoS One 3, e2078 (2008).
63. Svensson J.et al. Macrophages at the Fetal–Maternal Interface Express Markers of Alternative Activation and Are Induced by M-CSF and IL-10. J. Immunol 187, 3671–3682 (2011). [PubMed: 21890660]
64. Ścieżyńska Komorowski, Soszyńska & Malejczyk. NK Cells as Potential Targets for Immunotherapy in Endometriosis. J. Clin. Med 8, 1468 (2019). [PubMed: 31540116]

65. Nothnick WB Treating endometriosis as an autoimmune disease. Fertility and Sterility 76, 223–231 (2001). [PubMed: 11476764]
66. Malhotra D.et al. Transcriptional profiling of stroma from inflamed and resting lymph nodes defines immunological hallmarks. Nat. Immunol 13, 499–510 (2012). [PubMed: 22466668]
67. Rodda LB et al. Single-Cell RNA Sequencing of Lymph Node Stromal Cells Reveals Niche-Associated Heterogeneity. Immunity 48, 1014–1028.e6 (2018).
68. Csibi N.et al. Gamma-synuclein levels are elevated in peritoneal fluid of patients with endometriosis. Med. Sci. Monit 26, (2020).
69. Kang T-Y et al. Pericytes enable effective angiogenesis in the presence of proinflammatory signals. Proc. Natl. Acad. Sci. U. S. A 116, 23551–23561 (2019).
70. Egorova A.et al. Anti-angiogenic treatment of endometriosis via anti-VEGFA siRNA delivery by means of peptide-based carrier in a rat subcutaneous model. Gene Ther. 25, 548–555 (2018). [PubMed: 30254304]
71. Becker CM & D'Amato RJ Angiogenesis and antiangiogenic therapy in endometriosis. Microvascular Research 74, 121–130 (2007). [PubMed: 17574280]
72. Liu Z.et al. Single-cell transcriptomic analysis of eutopic endometrium and ectopic lesions of adenomyosis. Cell Biosci. 11, 1–17 (2021). [PubMed: 33407894]
73. Ma J.et al. Single-cell transcriptomic analysis of endometriosis provides insights into fibroblast fates and immune cell heterogeneity. Cell Biosci. 11, 1–19 (2021). [PubMed: 33407894]
74. Zou G.et al. Cell subtypes and immune dysfunction in peritoneal fluid of endometriosis revealed by single-cell RNA-sequencing. Cell Biosci. 11, 1–17 (2021). [PubMed: 33407894]

Methods References

75. Adam M, Potter AS & Potter SS Psychrophilic proteases dramatically reduce single-cell RNA-seq artifacts: A molecular atlas of kidney development. Dev. 144, 3625–3632 (2017).
76. Tan Y, Luo D, Bozal S, Robson P.& Courtois E.Human endometrium and endometriosis tissue dissociation for single-cell RNA sequencing. doi:10.17504/protocols.io.bvy8n7zw
77. Boretto M.et al. Patient-derived organoids from endometrial disease capture clinical heterogeneity and are amenable to drug screening. Nat. Cell Biol 21, 1041–1051 (2019). [PubMed: 31371824]
78. Turco MY et al. Long-term, hormone-responsive organoid cultures of human endometrium in a chemically defined medium. Nat. Cell Biol 19, 568–577 (2017). [PubMed: 28394884]
79. Stoeckius M.et al. Simultaneous epitope and transcriptome measurement in single cells. Nat. Methods 14, 865–868 (2017). [PubMed: 28759029]
80. Wolf FA, Angerer P.& Theis FJ SCANPY: large-scale single-cell gene expression data analysis. Genome Biol. 19, 15 (2018). [PubMed: 29409532]
81. Wolock SL, Lopez R.& Klein AM Scrublet: Computational Identification of Cell Doublets in Single-Cell Transcriptomic Data. Cell Syst. 8, 281–291.e9 (2019).
82. Giotti B.et al. Assembly of a parts list of the human mitotic cell cycle machinery. J. Mol. Cell Biol 11, 703–718 (2019). [PubMed: 30452682]
83. O'Flanagan CH et al. Dissociation of solid tumor tissues with cold active protease for single-cell RNA-seq minimizes conserved collagenase-associated stress responses. Genome Biol. 20, 210 (2019). [PubMed: 31623682]
84. Korsunsky I.et al. Fast, sensitive and accurate integration of single-cell data with Harmony. Nat. Methods 16, 1289–1296 (2019). [PubMed: 31740819]
85. Lavin Y.et al. Tissue-Resident Macrophage Enhancer Landscapes Are Shaped by the Local Microenvironment. Cell 159, 1312–1326 (2014). [PubMed: 25480296]
86. Becht E.et al. Dimensionality reduction for visualizing single-cell data using UMAP. Nat. Biotechnol 37, 38–44 (2019).
87. Traag VA, Waltman L.& van Eck NJ From Louvain to Leiden: guaranteeing well-connected communities. Sci. Rep 9, 5233 (2019). [PubMed: 30914743]
88. Ewels PA et al. The nf-core framework for community-curated bioinformatics pipelines. Nat. Biotechnol 38, 276–278 (2020). [PubMed: 32055031]

89. Lun ATL, Chen Y.& Smyth GK It's DE-licious: A Recipe for Differential Expression Analyses of RNA-seq Experiments Using Quasi-Likelihood Methods in edgeR. in Statistical Genomics, Methods in Molecular Biology 391–416 (Humana Press, 2016). doi:10.1007/978-1-4939-3578-9_19

90. Mootha VK et al. PGC-1α-responsive genes involved in oxidative phosphorylation are coordinately downregulated in human diabetes. Nat. Genet 2003 343 34, 267–273 (2003).

91. Subramanian A.et al. Gene set enrichment analysis: A knowledge-based approach for interpreting genome-wide expression profiles. Proc. Natl. Acad. Sci. U. S. A 102, 15545–15550 (2005).

92. Satija R, Farrell JA, Gennert D, Schier AF & Regev A.Spatial reconstruction of single-cell gene expression data. Nat. Biotechnol 33, 495–502 (2015). [PubMed: 25867923]

93. Tirosh I.et al. Dissecting the multicellular ecosystem of metastatic melanoma by single-cell RNA-seq. Science (80-.) 352, 189–196 (2016).

94. La Manno G.et al. RNA velocity of single cells. Nature 560, 494–498 (2018). [PubMed: 30089906]

95. Bergen V, Lange M, Peidli S, Wolf FA & Theis FJ Generalizing RNA velocity to transient cell states through dynamical modeling. Nat. Biotechnol 38, 1408–1414 (2020). [PubMed: 32747759]

96. Wolf FA et al. PAGA: graph abstraction reconciles clustering with trajectory inference through a topology preserving map of single cells. Genome Biol. 20, 1–9 (2019). [PubMed: 30606230]

97. Efremova M, Vento-Tormo M, Teichmann SA & Vento-Tormo R.CellPhoneDB: inferring cell–cell communication from combined expression of multi-subunit ligand–receptor complexes. Nat. Protoc 15, 1484–1506 (2020). [PubMed: 32103204]

98. Schindelin J.et al. Fiji: An open-source platform for biological-image analysis. Nature Methods 9, 676–682 (2012). [PubMed: 22743772]

99. Windhager J, Bodenmiller B.& Eling N.An end-to-end workflow for multiplexed image processing and analysis. BioRxiv (2021).

100. Schapiro D.et al. HistoCAT: Analysis of cell phenotypes and interactions in multiplex image cytometry data. Nat. Methods 14, 873–876 (2017). [PubMed: 28783155]

101. Ziegenhain C, Sandberg R.BAMboozle removes genetic variation from human sequence data for open data sharing. Nat Commun 12, 6216 (2021). [PubMed: 34711808]

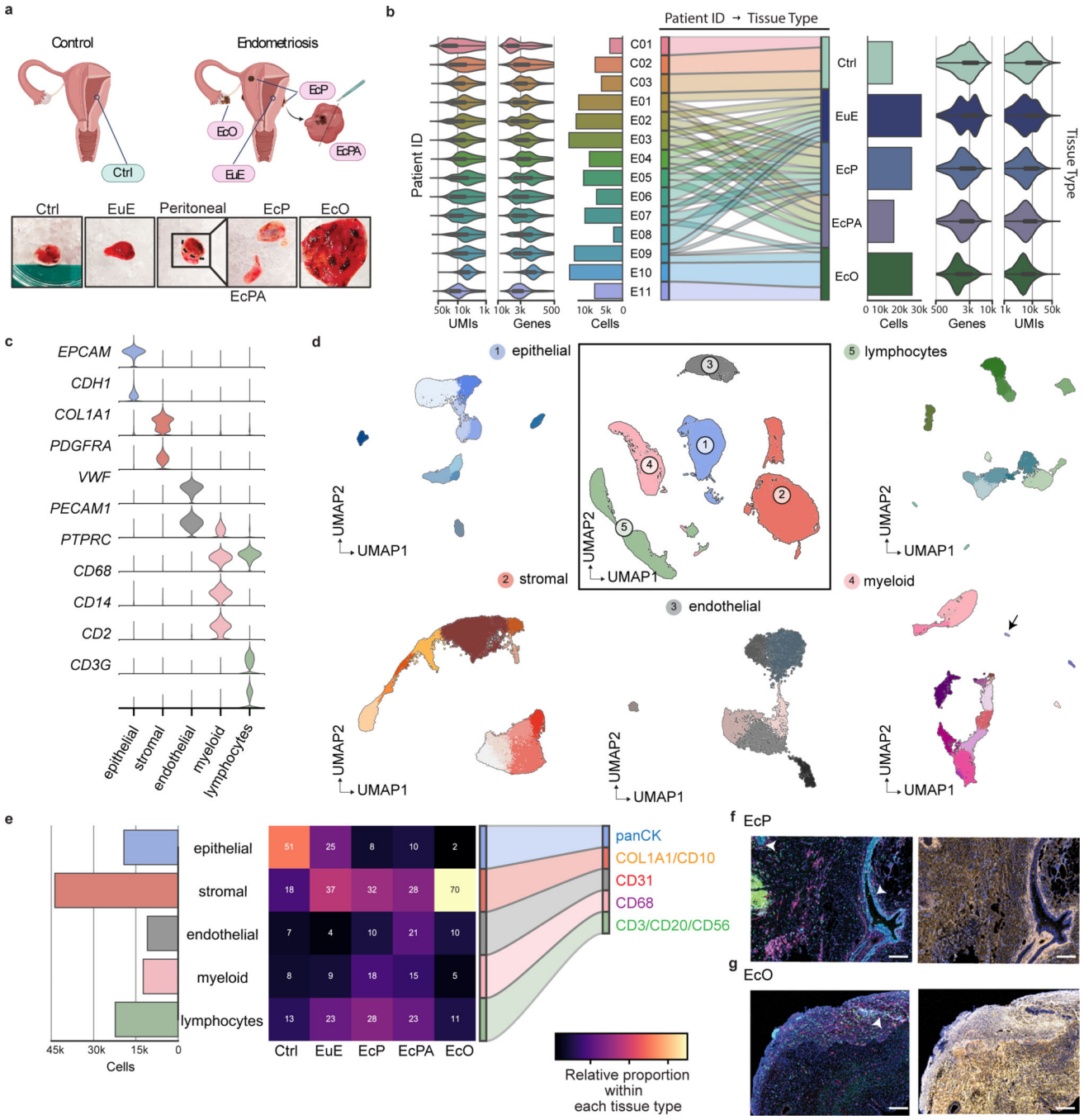

Fig. 1 |. scRNA-seq from control and endometriosis patient.

a, Schematic and photographic representation of collected tissue biopsies. Control (Ctrl) specimens were obtained from eutopic endometrium of women without endometriosis. Eutopic endometrium (EuE), ectopic peritoneal endometriosis (EcP), ectopic peritoneal adjacent lesion (EcPA), and ectopic ovarian endometriosis (EcO) were obtained from women with endometriosis. Peritoneal lesions were collected with a surrounding margin of up to 1 cm^2. The margin (EcPA) was separated upon macroscopic tissue assessment from the lesion (EcP) when possible and before single cell dissociation, as depicted in the

representative image for one biopsies. **b**, Diagram showing scRNA-seq metrics per patient (left) and tissue type (right) after QC. These metrics indicate unique molecular identifier (UMIs) and total genes per cells across patients and tissue types. The cord diagram (center) indicates the representation of each patient (E: endometriosis, C: control) in each tissue type. **c**, Violin plot representing marker gene expression for each major cell type identified in the scRNA-seq dataset. **d**, UMAP plot showing the 108,497 single-cells from control and endometriosis tissues. Five major cell types are identified (center UMAP plot) and subsequently subclustered into 58 subpopulations (radial UMAP plots). Each subpopulation was identified using marker genes curated form the literature. The presence of basophils and neutrophils (arrows) indicate that the cell recovery workflow was well-suited to capture delicate cell types known to be easily lost during tissue dissociation. **e**, Diagram showing number of major cell types (bar plot) and the cell type proportion in each tissue type (heatmap plot). Cell proportions are indicated within each square. Unique combinations of cell markers from each major cell cluster were used to design an IMC panel. Assigned colors represent each major cell type identified in EcP (**f**) and EcO (**g**). White arrows indicate endometriotic epithelial glands. Scale bar = 100 μm.

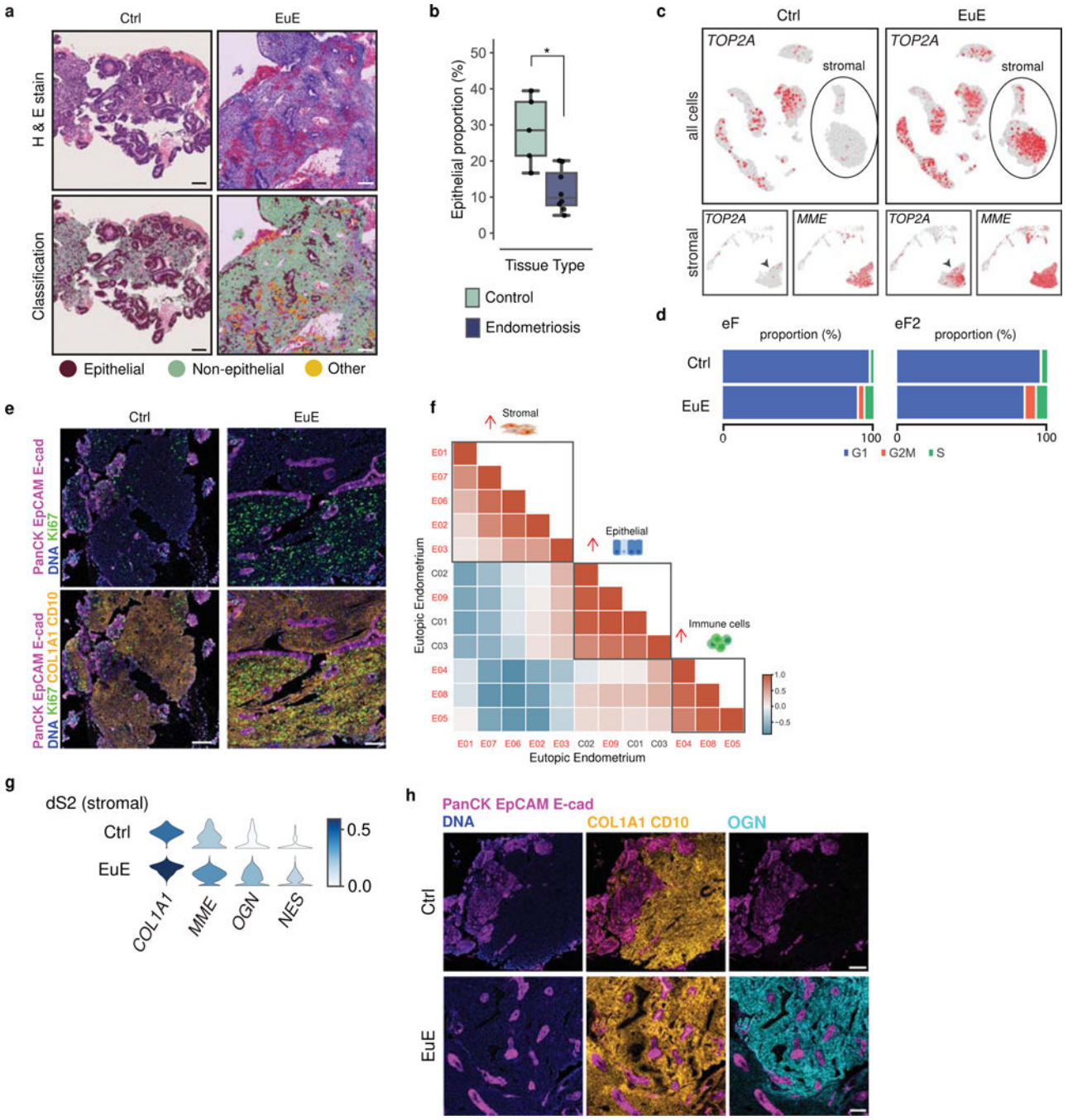

Fig. 2. |. Cellular composition of Ctrl and endometriosis eutopic endometrium.

a, Representative H&E images of eutopic tissues from Ctrl (n=5) and EuE (n=8), before and after classification. **b**, Box plot showing the proportion of epithelial cells in endometrial tissue. Ctrl (n=5) tissues show significantly higher epithelial cell proportion compared to EuE (n=8), Welch's T-test, two-sided, p-value = 0.013. Each dot represents a tissue section; See Source Data Fig2. Box represents the interquartile range, whiskers represent min and max, and box centerline represents median. **c**, UMAP representation for the expression of *TOP2A* in Ctrl and EuE in global clustering (top). Circle denotes the stromal

cell population. Representation of *TOP2A* (proliferating cells) and *MME* (endometrial fibroblasts) expressing cells in Ctrl and EuE stromal subclusters (bottom). Arrows depict all endometrial fibroblast (eF) expressing *TOP2A* in EuE. **d**, Proportion of cells in G1, G2M, S cell cycle phases within all eF and in eF2 subpopulation. **e**, Representative IMC image showing the presence of proliferating cells labelled with KI67 (green) in Ctrl (n=4) and EuE (n=5); epithelial cells marked with PanCK, EpCAM, E-cadherin (magenta); stromal cells marked with COL1A1 and CD10 (yellow/orange); nuclei marked with DNA (blue). **f**, Matrix plot representing the overall similarity of endometrium biopsies from control and endometriosis (Pearson correlation based on gene expression from each patient). EuE clustered into two groups, each showing an enrichment of fibroblasts or immune cells (E: endometriosis, C: control). **g**, Violin plot showing significantly upregulated genes (*OGN* and *NES*) in EuE relative to Ctrl in decidualized stroma (dS2) subpopulation. **h**, Representative IMC image confirming increase of OGN (cyan) secretion within stroma (orange) in EuE (n=5) relative to Ctrl (n=4). **a**, **e**, **h**, Both Ctrl and EuE representative images are taken from patient receiving same hormonal treatment, Scale bar = 100 μm.

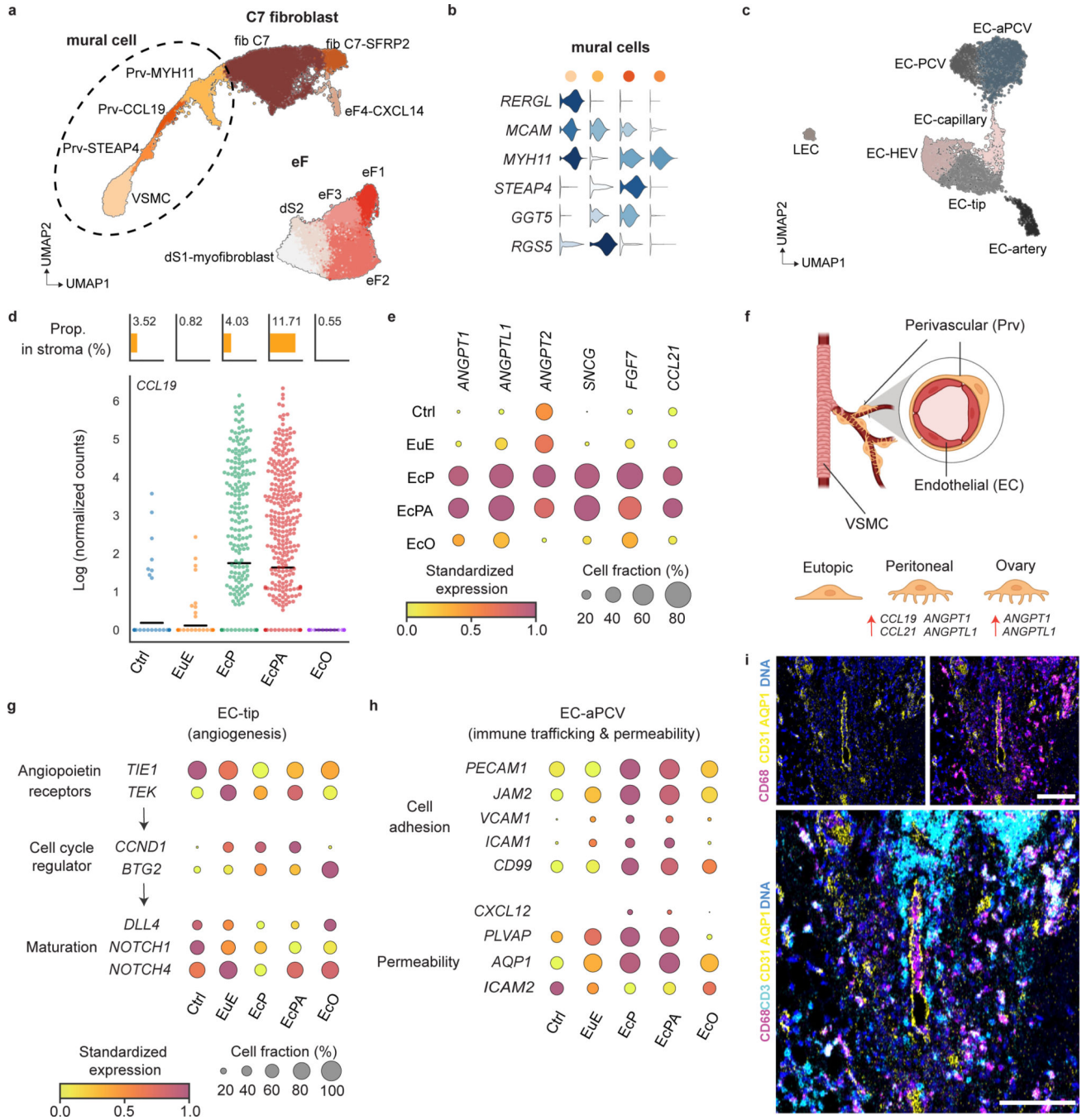

Fig. 3 |. Role of Stromal cell diversity in angiogenesis and immune trafficking in endometriosis lesions.

a, UMAP plot of the 12 identified stromal subpopulations and classified into three general cell subtypes: endometrial fibroblast (eF), C7 fibroblast (fib C7) and mural cell (n = 42,713 cells). **b**, Violin plot showing markers of mural cell subpopulations. **c**, UMAP plot of endothelial cells (EC), represented across 7 subclusters: lymphatic EC (LEC), high endothelial venule (EC-HEV), tip EC (EC-tip), capillary (EC-capillary), post-capillary vein (EC-PCV), activated PCV (EC-aPCV), and arterial (EC-artery). **d**, (top) Proportion of Prv-

CCL19 within stromal cells. A major increase of Prv-CCL19 is observed in EcPA. Bars represent the mean value. (bottom) The swarm plot shows *CCL19* expression in individual cells from each lesion. **e**, Dot plot showing significantly upregulated genes involved in angiogenesis and immune cell trafficking (edgeR, FDR < 0.05) in Prv-CCL19. **f**, Schematic of mural and EC localization. Larger arteries and veins are unsheathed by VSMC, while smaller vessels (e.g., capillaries) are unsheathed by perivascular cells. Lesions Prv cells increase expression of pro-angiogenic genes when compared to Ctrl. **G**, Dot plot showing significant representative DEGs involved in new vessel formation in tip EC (edgeR, FDR <0.05). **h**, Dot plot showing significant DEGs involved in cell adhesion and permeability in a-PCV (edgeR, FDR <0.05). **I**, Representative IMC image from a peritoneal lesion (n=7). $CD3^+$ T-cells (cyan) and $CD68^+$ myeloid cells (magenta) localize within and surrounding blood EC vasculature marked by CD31 and AQP1 (yellow). Nuclei counterstained by DNA labeling (blue). Scale bar = 100μm.

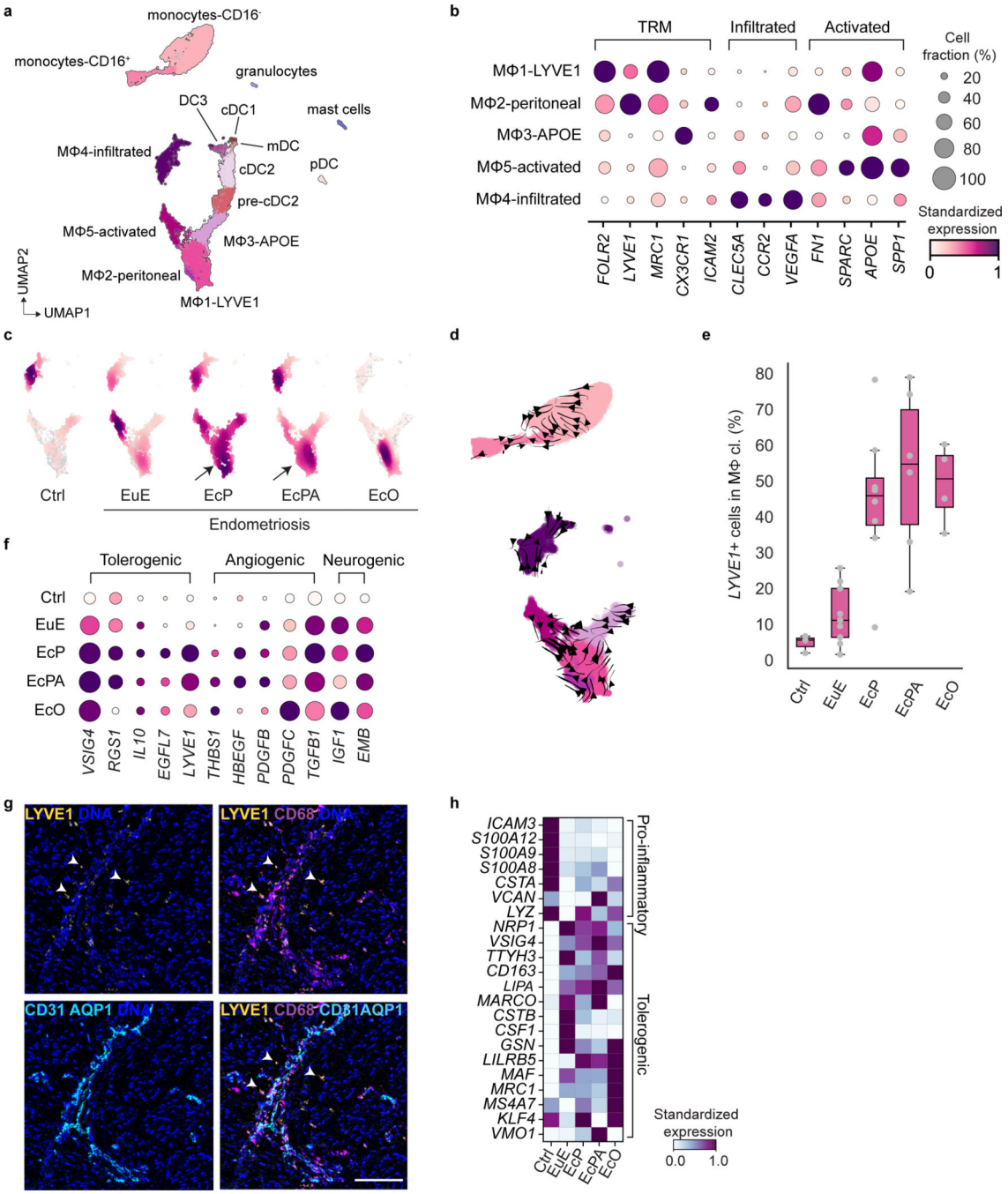

Fig. 4 |. Macrophage heterogeneity in control and endometriosis.

a, UMAP plot of myeloid cells, clustered into 15 different subtypes (n = 12,262 cells). **b**, Dot plot showing expressed marker genes for tissue-resident (TRM), blood-infiltrated, and activated macrophages across identified Mϕ subpopulations and tissues. **c,** Density plot showing macrophage distribution for in each tissue type. **d,** UMAP plot showing RNA velocity streamlines for monocytes and macrophages in Ctrl. Streamlines represent the predicted transition path of cells across subpopulations. **e,** Bar plot showing the proportion of *LYVE1*-expressing cells to all macrophages within each tissue type. Each dot represent

percentage of LYVE1+ cells in a tissue biopsy (Ctrl n = 3, EuE n = 9, EcP n = 8, EcPA n = 6, EcO n = 4). The box represents the interquartile range with median and minimum/maximum represented by box centerline and whiskers, respectively. **f,** Dot plot showing DEG involved in immunotolerance in Mϕ1-LYVE1 population. **g,** IMC image from FFPE tissue section of a peritoneal lesion. Images depict $LYVE1^{+}$ macrophages (LYVE1, CD68) localization near endothelial cells (CD31, AQP1) (white arrows). Scale bar =100μm. **h,** Matrix plot showing expression of pro-inflammatory and pro-tolerogenic related genes in Mϕ4 subpopulation in Ctrl and endometriosis.

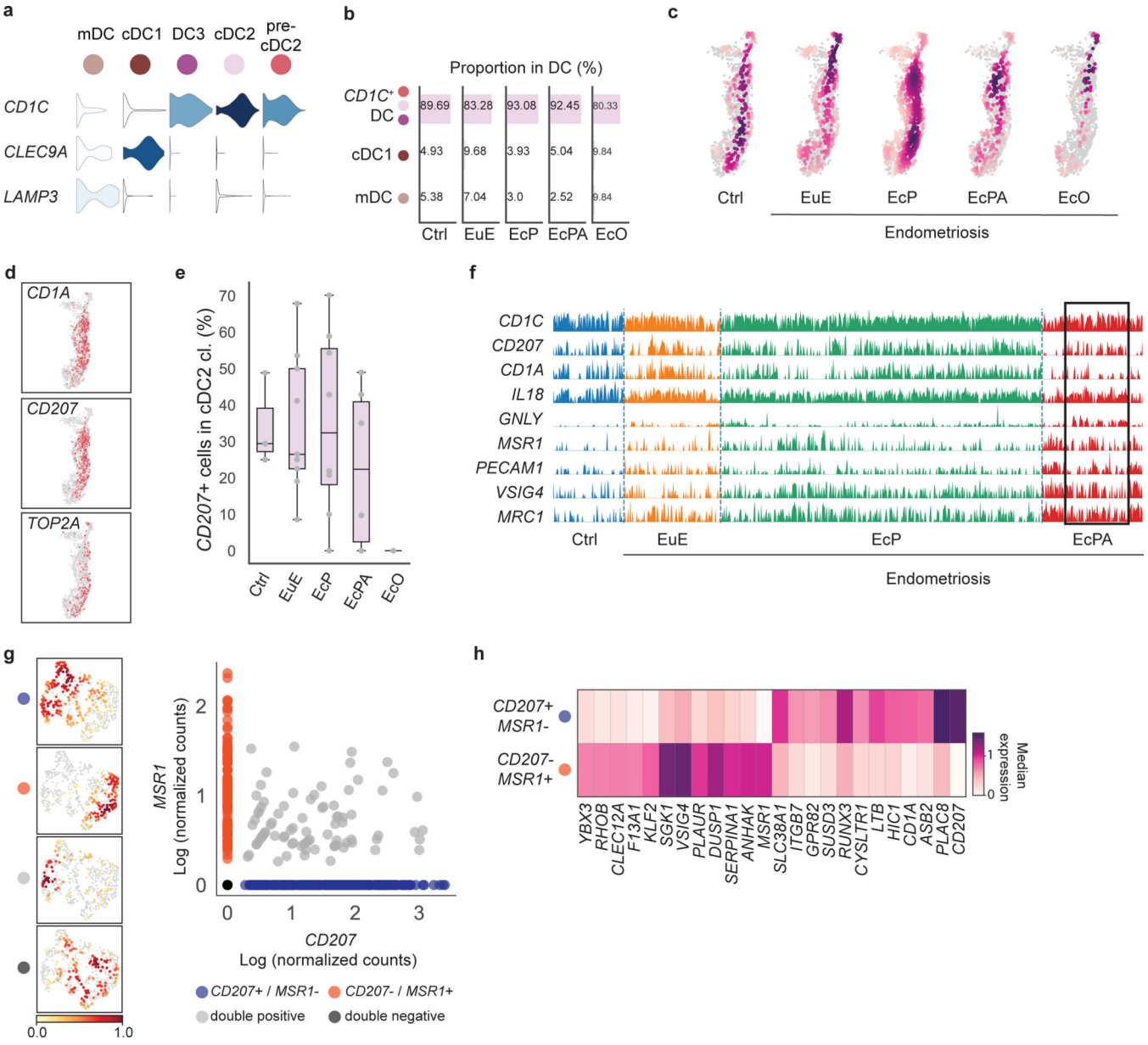

Fig. 5 |. Immunomodulatory role of DC in peritoneal endometriosis.

a, Violin plot showing markers of dendritic cell (DC) subpopulations; *CD1C* expression is prevalent in three DC subpopulations: pre-cDC2, cDC2 and DC3. **b**, *CD1C*$^{+}$cells represent majority of the DC population, accounting for more than 83% of DCs in all but ectopic ovary tissue. **c**, Density plot showing the increased cDC2 populations in peritoneal lesions compared to EuE. **d**, Expression of cDC2 markers *CD207* and *CD1A;* and proliferation marker *TOP2A.* **e**, Proportion of *CD207* expressing cells across all cDC2 populations. *CD207*+ cells were consistently observed in eutopic endometrium, but variable in peritoneal lesions and not observed in ovarian lesions. Each dot represents the percentage of CD207^{+} for each tissue biopsy (Ctrl n = 3, EuE n = 9, EcP n = 8, EcPA n = 6, EcO n = 4). The box represents the interquartile range with median and minimum/maximum represented by box centerline and whiskers, respectively. **f**, Track plot representing the expression of DEGs

upregulated in cDC2-CD1A in EcPA (Wilcoxon, FDR < 0.05). Each bar represents a cell. Differential expression for the represented genes is detected in EcPA cells (black box). **g**, Density plot of cDC2 from EcP and EcPA showing the distribution of cDC2 on UMAP representing different cell states (left). *S*catter plot showing *CD207+/MSR1-* (n = 237), *CD207-/MSR1+* (n = 121), double positive (n = 82) and double negative (n = 141) cells (right). **h**, Top 12 DEGs between *CD207+/MSR1-* and *CD207-/MSR1+* populations from cDC2 subpopulations in EcP and EcPA (Wilcoxon, FDR < 0.05, logFC > 1).

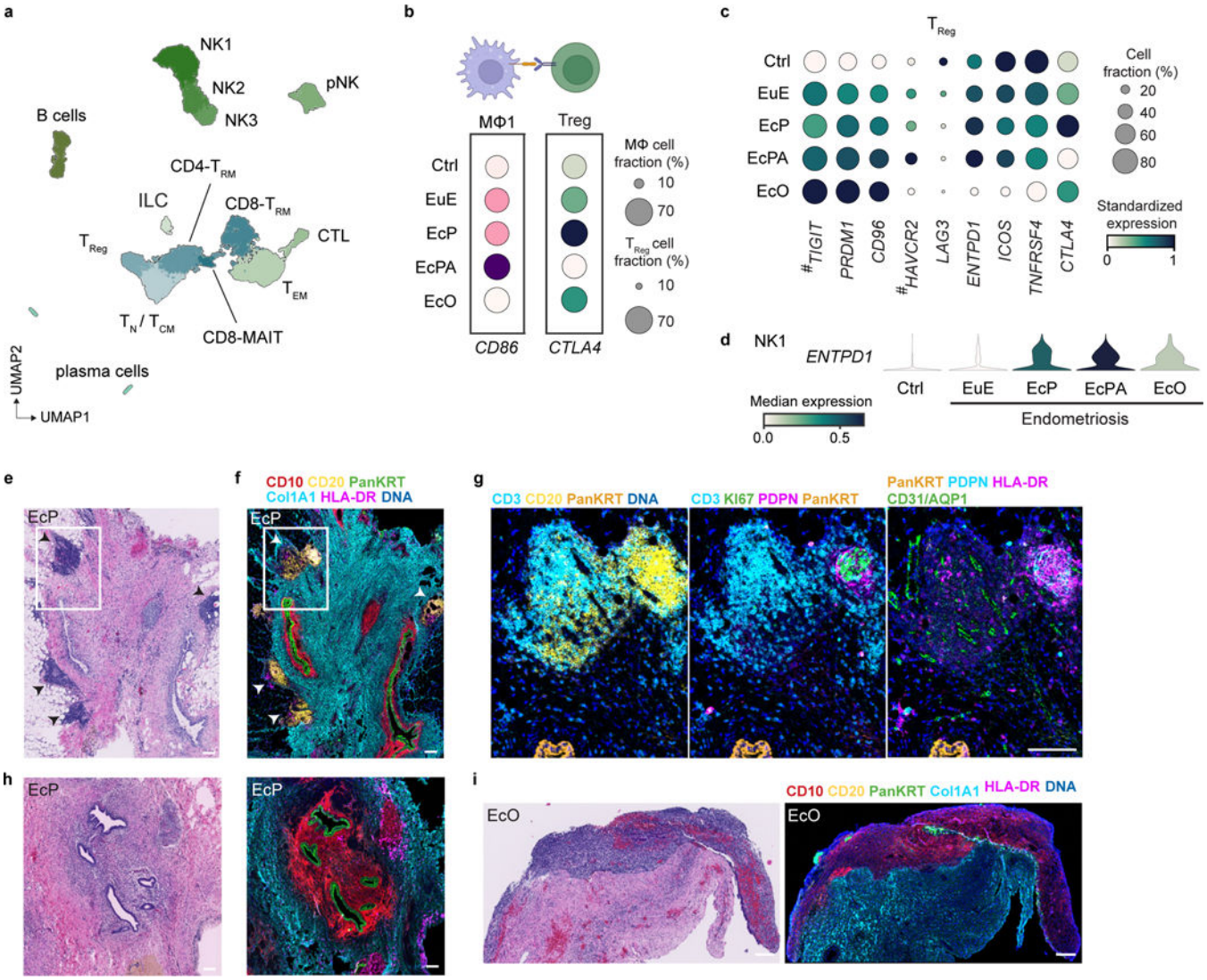

Fig. 6 |. TLS presence in peritoneal endometriosis.

a, UMAP plot of lymphocyte subpopulations. Represented clustering highlights 14 different subpopulations (n=22,225) based on known markers. **b**, Schematic showing CD86-CTLA4 ligand-receptor interaction between macrophages MΦ1 and Tregs. The dot plot shows gene expression for this interacting pair in each tissue type. **c,** Dot plot showing DEGs associated with T_{Reg} self-tolerance maintenance (edgeR, FDR <0.05, # marks non-significant DEG). **d,** Violin plot representing *ENTPD1* gene expression in tissue-resident NK1 cells across sample types. **e**, H/E staining from FFPE tissue section of a peritoneal lesion. This patient sample presented TLS-like formation highlighted in the white frame, detected in n=2 out of 7 EcP. **f,** IMC image from the same lesion showing endometrial fibroblasts (CD10, red), B-cells (CD20, yellow), epithelial cells (Pan-KRT, green), stroma (Col1A1, cyan) and antigen presenting cells (HLA-DR, magenta). TLS are primarily located through an accumulation of $CD20^+$ cells forming GC-like structures in the periphery of the lesion (white frame, arrow). HLA-DR overlap with CD20 indicates an antigen presenting capacity within the GC. **g**, Magnified image showing GC structures with accumulation of B-cells (CD20, yellow) in the

center surrounded by T-cells (CD3, cyan). KI67 labels proliferative B-cells within the GC (green, middle). CD31 and AQP1 label blood endothelial cells (green, right panel). PDPN marks follicular dendritic cells (magenta on middle or cyan on right image). **h-i**, H/E (left) and corresponding IMC (right) representative images from endometriotic lesions without TLS in EcP (n=5/7) (**h**) and EcO (n= 6/6) (**i**) for identical antibodies panels in (**f**). Scale bar =100 μm.

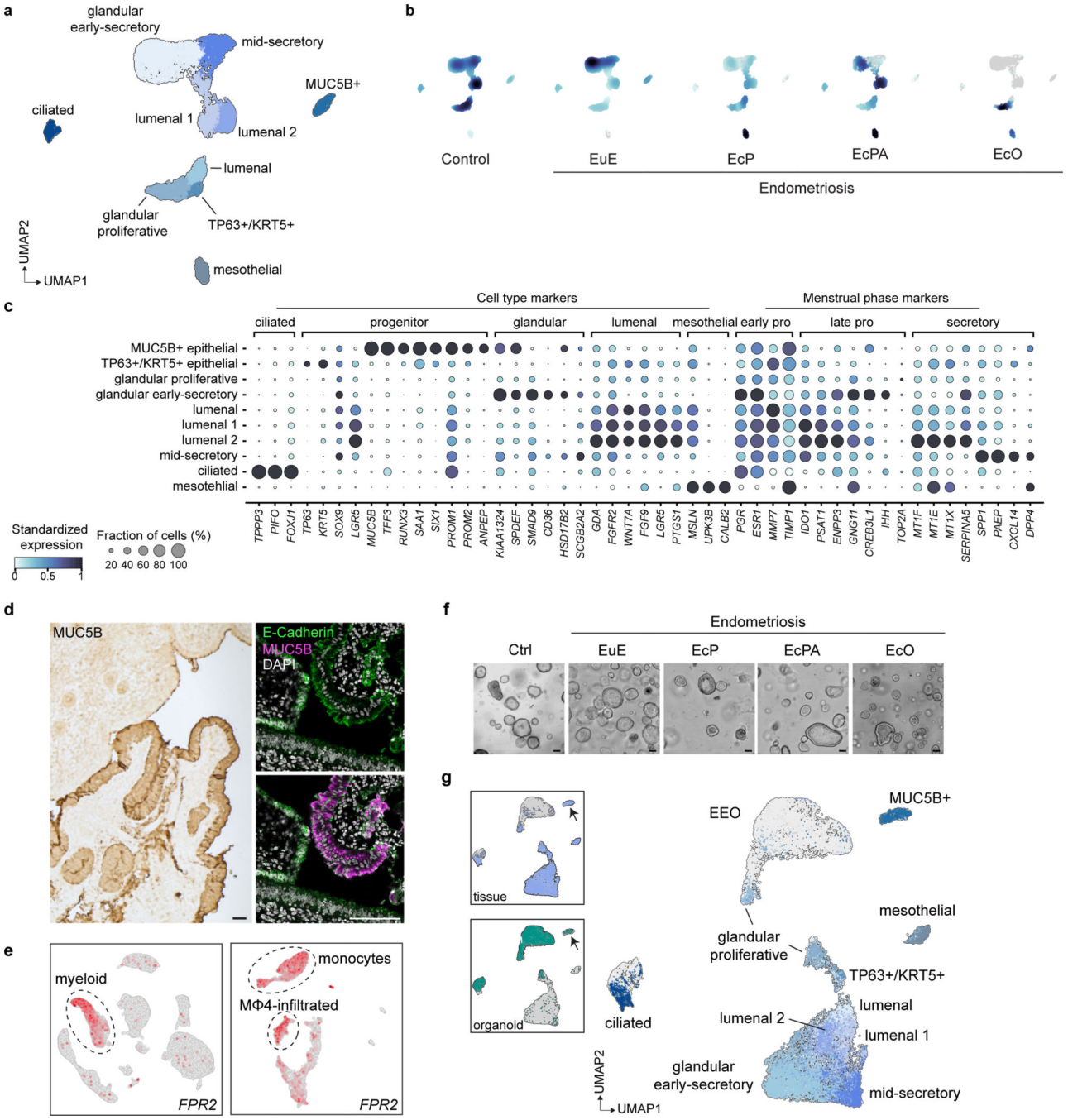

Fig. 7 |. Characterization of epithelial cell subpopulations in Ctrl and endometriosis patients.
a, Unsupervised clustering of epithelial cells led to 10 subpopulations (n=19,200) represented in the UMAP. **b**, Density plot showing the distribution of epithelial subtypes across tissues. **c**, Markers for each epithelial subtype and menstrual phase across each epithelial cell subtype. **d**, Immunohistochemistry (IHC) staining confirms the presence of MUC5B^{+} cells in EuE (Left panel, n = 1). Immunofluorescence (IF) showing co-localization of endometrial epithelial (E-Cadherin^{+}, in green) and MUC5B^{+} cells (magenta). Nuclei were counterstained with DAPI (cyan) in EuE (n = 4). Scale bar = 100μm. **e**, Formyl

Peptide Receptor 2 (*FPR2)* expression is specific to myeloid cells (left), and more precisely to monocytes and Mϕ4-infiltrated cells (right). **f**, Representative image of endometrial epithelial organoid (EEO) cultures derived from dissociated single cell of endometrium and endometriotic lesions. **g**, UMAP plot representing the merge dataset for *in vivo* (tissue derived) and *in vitro* (EEO) epithelial cells. Classification follows previously described subpopulations *in vivo*.